

國立交通大學
光電工程研究所
碩士論文

利用伽瑪氧化鋁為緩衝層成長於(111)矽晶圓的

氧化鋅磊晶薄膜之結構與光性研究

**Structural and optical properties of ZnO
epi-layer grown on Si(111) using a γ -Al₂O₃
buffer layer**

研究生：李岳勳

指導教授：徐嘉鴻教授

謝文峰教授

中華民國九十七年六月

利用伽瑪氧化鋁為緩衝層成長於(111)矽晶圓的
氧化鋅磊晶薄膜之結構與光性研究

**Structural and optical properties of ZnO
epi-layer grown on Si(111) using a γ -Al₂O₃
buffer layer**

研 究 生：李岳勳

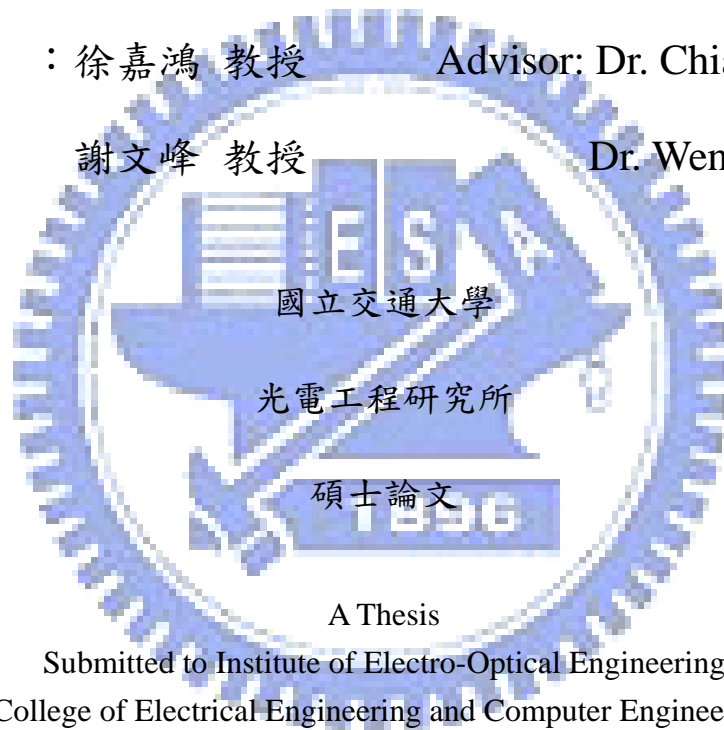
Student: Yueh-Hsun Li

指導教授：徐嘉鴻 教授

Advisor: Dr. Chia-Hung Hsu

謝文峰 教授

Dr. Wen-Feng Hsieh



A Thesis

Submitted to Institute of Electro-Optical Engineering
College of Electrical Engineering and Computer Engineering

National Chiao Tung University

in Partial Fulfillment of the Requirements

for the Degree of

Master

in

Electro-Optical Engineering

June 2008

Hsinchu, Taiwan, Republic of China

中華民國九十七年六月

利用玳瑁氧化鋁為緩衝層成長於(111)矽晶圓的氧化鋅磊晶薄膜之結構與光性研究

研究生：李岳勳

指導教授：徐嘉鴻教授

謝文峰教授

國立交通大學電機學院光電工程研究所

摘要

藉由一層玳瑁氧化鋁緩衝層將高品質氧化鋅薄膜以雷射濺鍍方法磊晶成長於(111)面的矽晶圓上，此玳瑁氧化鋁緩衝層含有以晶面(111)為軸向的兩種彼此旋轉 60 度的結構空間分布。樣品在垂直表面方向的磊晶結構關係為氧化鋅(0002)//玳瑁氧化鋁{22-4}或{4-2-2}//矽晶圓{22-4}。利用 X 光繞射、穿透式電子顯微鏡與螢光光譜來量測氧化鋅的晶體結構與光學特性，我們發現深層能階發光的強度相對於能隙發光強度比與薄膜的 ϕ 角半高寬大小有明顯的關聯；而能隙發光光譜的半高波寬分布大小與薄膜的表面晶面方向分布有關。這個關聯也就代表螺旋型差排缺陷主要與能隙發光光譜有關，而邊刀型差排缺陷主要與深層能階發光有關。

Structural and optical properties of ZnO epi-layer grown on Si(111) using a γ -Al₂O₃ buffer layer

Student: Yueh-Hsun Li

Advisors: Prof. Chia-Hung Hsu

Prof. Wen-Feng Hsieh

Institute of Electro-Optical Engineering

National Chiao Tung University

Abstract

High-quality ZnO epitaxial films were grown by pulsed-laser deposition on Si(111) substrates with a thin γ -Al₂O₃ buffer layer. The epitaxial γ -Al₂O₃ buffer layer consists of two (111) oriented domains rotated 60° from each other against the surface normal. Therefore, two in-plane epitaxial relationships $\{10\bar{1}0\}_{\text{ZnO}} \parallel \{22\bar{4}\}_{\gamma\text{-Al}_2\text{O}_3} \parallel \{22\bar{4}\}_{\text{Si}}$ and $\{10\bar{1}0\}_{\text{ZnO}} \parallel \{4\bar{2}2\}_{\gamma\text{-Al}_2\text{O}_3} \parallel \{22\bar{4}\}_{\text{Si}}$ coexist. The crystalline quality and optical properties of ZnO epi-layers were studied by x-ray diffraction, transmission electron microscopy and photoluminescence measurements. A clear correlation between the intensity ratio of ZnO deep-level emission (DLE) to near-band edge (NBE) emission and the width of the ϕ -scan across off-normal reflection was observed. The NBE linewidth also exhibits a strong dependence on the width of the ZnO (0002) rocking curve. These observations indicate the NBE and the DLE emissions are mainly affected by the screw and the edge type threading dislocations, respectively.

誌謝

時間過得真快，兩年就這樣過去了，回想這七百多個日子裡真是嘗盡了心酸也充滿了歡笑，也在這點點滴滴的過程中學到了不少；首先要非常感謝我的指導教授徐嘉鴻老師以及教授謝文峰老師的指導，在老師們的指導下讓我在知識上獲益良多，還有維仁學長的指教和領導，同時也很感謝由洪銘輝教授以及郭瑞年教授所帶領的清華大學材料所先進奈米磊晶實驗室所提供的試片，以及實驗室和同步輻射研究中心的所有學長姐學弟妹同儕們的幫忙，讓我可以很充實很順利地度過這兩年的時光，同時也感謝國科會計畫(計畫編號：NSC-96-2119-M-213-003 和 NSC-96-2628-M-009-001-MY3)的贊助，讓我可以專心於實驗。

最後要感謝我的父母親友們，謝謝你們這些年來源源不絕給我的支持和愛護，讓我在學業以及生活上獲益良多。

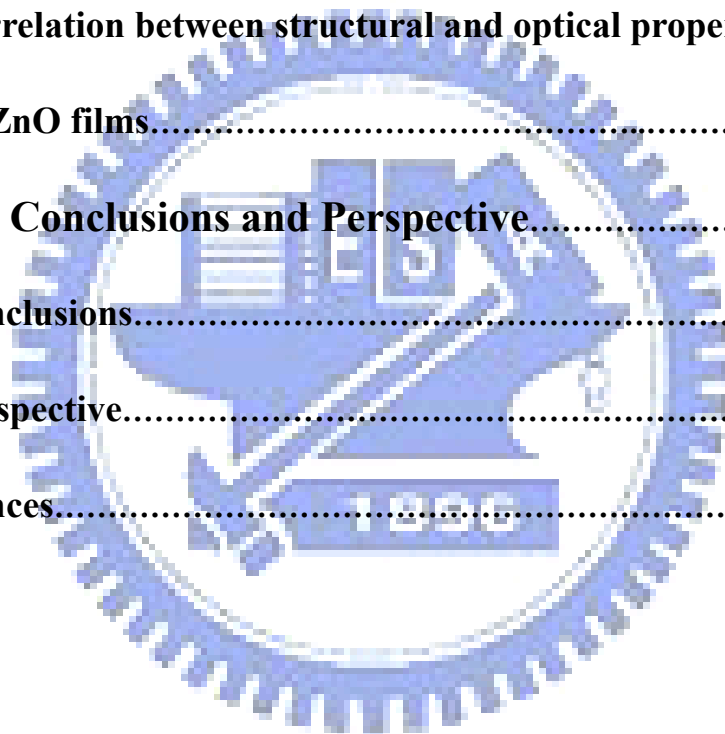


Content

Chinese Abstract.....	i
English Abstract.....	ii
Acknowledgement.....	iii
Contents.....	iv
List of Figures.....	vii
List of Tables.....	ix
Chapter 1 Introduction.....	-1-
1-1 A brief review.....	-1-
1-2 Motivation.....	-2-
1-3 Organization of the thesis.....	-4-
Chapter 2 Theoretical background.....	-5-
2-1 The laser-MBE system and principle of laser-MBE Deposition.....	-5-
2-2 X-ray diffraction.....	-8-
2-2-1 Theory of x-ray diffraction.....	-8-
2-2-2 Rocking curve.....	-11-
2-2-3 Phi scan.....	-11-
2-2-4 Analysis of threading dislocation density.....	-12-

2-3 Transmission electron microscopy.....	-16-
2-3-1 Selected area electron diffraction (SAED).....	-17-
2-3-2 Analysis of threading dislocation density.....	-18-
2-4 Photoluminescence characterization.....	-22-
2-4-1 Fundamental Transitions.....	-23-
Chapter 3 Experimental details.....	-26-
3-1 The growth of ZnO films.....	-26-
3-1-1 Description of laser-MBE system.....	-26-
3-1-2 The layout of laser-MBE system.....	-27-
3-1-3 Target preparation.....	-28-
3-1-4 Preparation of substrate.....	-28-
3-1-5 Operating process of laser-MBE.....	-29-
3-2 Structural characterization of the ZnO films.....	-31-
3-2-1 X-ray diffraction.....	-31-
3-2-2 Cross sectional TEM.....	-32-
3-3 Measurements of optical properties.....	-33-
3-3-1 Photoluminescence detection system.....	-33-
Chapter 4 Results and Discussion.....	-35-
4-1 Results of X-ray measurements.....	-35-
4-1-1 Growth temperature dependent crystallinity of the ZnO films..	-35-

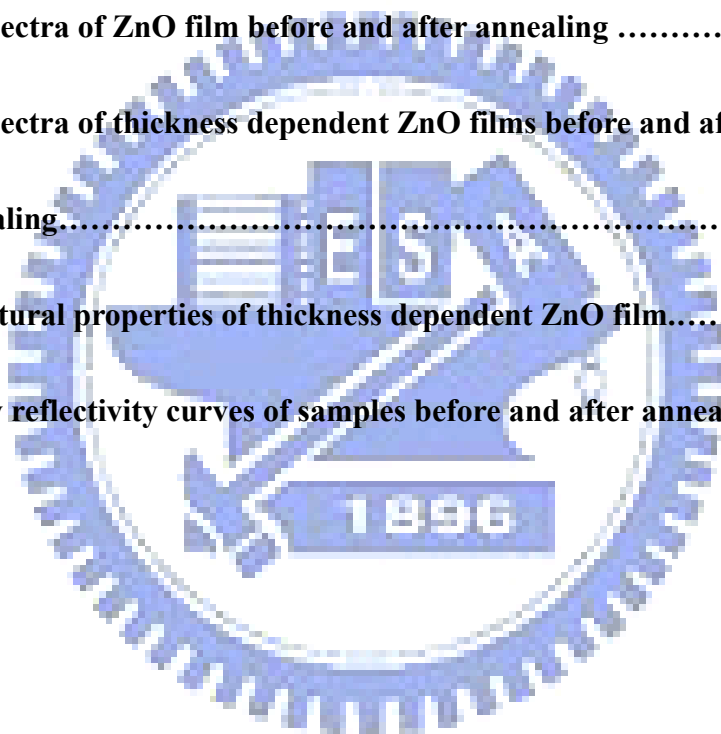
4-1-2 Analysis of threading dislocation density by XRD.....	41-
4-2 Structural characterization by TEM.....	46-
4-2-1 Cross sectional TEM.....	46-
4-2-2 Analysis of threading dislocation density.....	48-
4-3 Optical characterization by PL.....	51-
4-3-1 photoluminescence spectra of as-grown film.....	51-
4-4 Correlation between structural and optical properties	
of ZnO films.....	55-
Chapter 5 Conclusions and Perspective.....	59-
5-1 Conclusions.....	59-
5-2 Perspective.....	59-
References.....	68-



List of Figures

Fig. 1-1 Wurtzite structure.....	2
Fig. 2-1 Schematic of a laser-MBE growth system.....	7
Fig. 2-2 X-ray scattering from a cubic crystal.....	10
Fig. 2-3 The hexagonal unit cell.....	10
Fig. 2-4 Illustration of phi scan.....	11
Fig. 2-5 Illustration of Burgers vector and types of dislocations.....	16
Fig. 2-6 The TEM image contrast of a wedge-shaped specimen.....	21
Fig. 2-7 Radiative transitions between a band and an impurity state.....	25
Fig. 3-1 Layout of laser-MBE system.....	27
Fig. 3-2 The preparation process of a cross-sectional TEM specimen.....	33
Fig. 3-3 Layout of PL system.....	34
Fig. 4-1 Radial scan along the surface normal of a sample.....	37
Fig. 4-2 The profile of ϕ -scans across ZnO {10-10}, γ -Al ₂ O ₃ (440) and Si{220} reflections.....	37
Fig. 4-3 Correlation between growth temperature and ZnO structural quality..	40
Fig. 4-4 Williamson-Hall plots of ZnO layers.....	44
Fig. 4-5 Williamson-Hall plots for transverse scans.....	45
Fig. 4-6 Selected area electron diffraction pattern and HR-TEM image.....	47
Fig. 4-7 Two-beam bright field cross sectional micrograph.....	50

Fig. 4-8 Typically PL spectra measured at 15K for ZnO epi-layers.....	53
Fig. 4-9 The extended spectra of NBE emission of ZnO film.....	54
Fig. 4-10 Dependence of PL FX_A peak intensity on sample temperature.....	54
Fig. 4-11 Correlation between structural and optical properties.....	57
Fig. 4-12 Correlation between threading dislocation densities and optical properties.....	58
Fig. 5-1 PL spectra of ZnO film before and after annealing	64
Fig. 5-2 PL spectra of thickness dependent ZnO films before and after annealing.....	65
Fig. 5-3 Structural properties of thickness dependent ZnO film.....	66
Fig. 5-4 X-ray reflectivity curves of samples before and after annealing.....	67



List of tables

Table 3-1 LPX210i (KrF) specifications.....28



Chapter 1 Introduction

1-1 A brief review

Zinc oxide is a crystal of hexagonal wurtzite structure with the lattice constants of $a = 3.24 \text{ \AA}$ and $c = 5.20 \text{ \AA}$ as shown in Fig. 1-1. ZnO has been considered as one of the most promising candidates for the materials used in short-wavelength photonic devices because of its wide band gap of 3.37 eV and large exciton binding energy of 60 meV at room temperature [1]. In contrast to technical limitations of GaN (band gap = 3.4eV), exciton of ZnO is stable even at elevated temperature. Recently, the strong commercial desire for blue and ultraviolet diode lasers and light emitting diodes has prompted enormous research efforts into II-VI wide band gap semiconductors [2]. In 1997, Y. F. Chen, et al. [3] demonstrated the lasing from ZnO epilayers grown by MBE with the threshold intensity of 240 KW/cm^2 . In 1998, Kawasaki et al. [4], found laser operation of ZnO thin film at room temperature grown using laser-molecular beam epitaxy. The lasing mechanism is attributed to the exciton-exciton collision process.

In order to obtain good quality of ZnO thin film, several growth technologies have been used such as molecular-beam exptaxy (MBE) [5], metal-organic chemical vapor deposition (MOCVD) [6], and laser molecular-beam epitaxy (LMBE) [7]. Among these methods, LMBE has the advantages of ultra-clean, simplicity, without corrosive

gas, and achieving high-quality epitaxial films at a relatively low growth temperature (220 °C~500 °C) due to its high kinetic energy (10 eV~100 eV) of laser ablated species. Besides, the source of Zn and O can be obtained directly from the target, i.e. no extra oxygen supply is necessary. This process is important for some devices since the oxygen atmosphere during the laser ablation leads to several problems, such as the oxidation of the internal parts in the chamber.

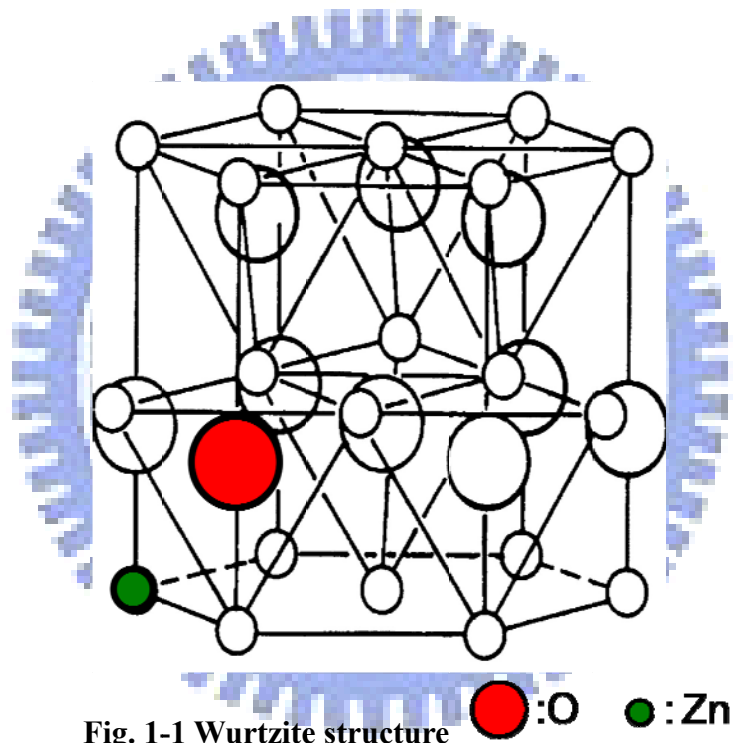


Fig. 1-1 Wurtzite structure

1-2 Motivation

Recently, much attention has been paid to heteroepitaxially grown ZnO on Si substrates because of the unique possibility of integrating well-established Si electronics with ZnO-based optoelectronic devices. Unfortunately, direct growth of epitaxial ZnO

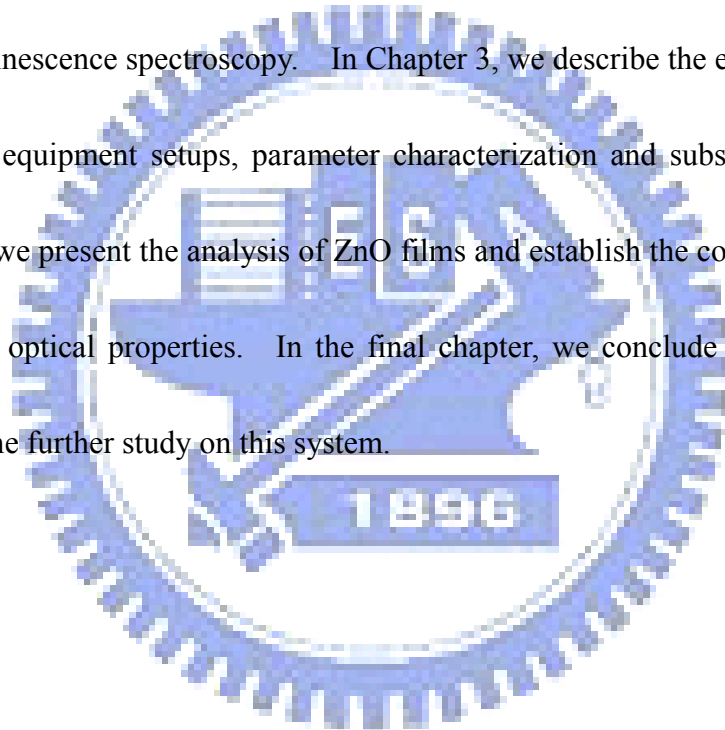
films on Si is an extremely difficult task due to the formation of an amorphous SiO₂ layer at the ZnO/Si interface [8, 9] that usually results in polycrystalline films with preferred orientation [10]. Although significant efforts have been made to use nonoxide materials, such as ZnS [8], Si₃N₄ [9], Zn/MgO [11] and Mg/MgO [12], as buffer layers, the growth of high-quality ZnO epi-films on Si is still regarded as an arduous challenge.

The other issue for the growth of high-quality ZnO epi-films is the existence of high-density threading dislocations (TDs) originating from the large difference in the lattice mismatch (-15.4%) and the thermal expansion coefficient (56%) between ZnO (thermal expansion coefficient $\alpha \sim 5 \times 10^{-6} \text{ K}^{-1}$ [13], lattice parameters $a = 3.24 \text{ \AA}$, $c = 5.20 \text{ \AA}$) and the underneath Si substrate ($\alpha = 3.6 \times 10^{-6} \text{ K}^{-1}$ [14], $a = 5.431 \text{ \AA}$). The point defects captured by TDs stress field act as traps and recombination sites forming deep electronic states inside the band gap [15, 16]. They can lead to electron scattering [17], significantly affect the optical performance and electron mobility [16, 18] and adversely demote the device efficiency. In this thesis, we report the growth of high-quality epitaxial ZnO films using pulsed-laser deposition (PLD) on Si (111) substrates with a ~15.3 nm thick γ -Al₂O₃ film as the buffer layer. The good crystal structure of thin ZnO films was confirmed by x-ray diffraction (XRD) and transmission electron microscopy (TEM). Their optical characteristics were studied using

photoluminescence (PL) and correlated with the structural properties.

1-3 Organization of the thesis

The thesis consists of five chapters. In Chapter 2, we review the background mechanism of Laser-MBE as well as the basic theory of the characterization tools employed semiconductor such as X-ray diffraction, transmission electron microscopy and photoluminescence spectroscopy. In Chapter 3, we describe the experiment details, including the equipment setups, parameter characterization and substrate preparation. In Chapter 4, we present the analysis of ZnO films and establish the correlation between structural and optical properties. In the final chapter, we conclude our investigation and propose the further study on this system.



Chapter 2 Theoretical background

2-1 The laser-MBE system and principle of laser-MBE deposition

Figure 2-1 illustrates the schematic of a laser-MBE deposition system. Laser beam is shined on the target material. The high heating power leads to the evaporation of the target material, forming a high-temperature plasma plume that expands away from the target surface. The ablated target material is deposited on a substrate and forms a thin film. Depending on the types of interaction of the laser beam with target, the laser deposition process can be classified into three parts:

i. Interaction of laser beam with the target

Upon being struck by a high power density nanosecond excimer-laser pulse, heating and vaporizing the material will occur at the beginning of the pulse. The amount of evaporated flux varies linearly with the pulse energy.

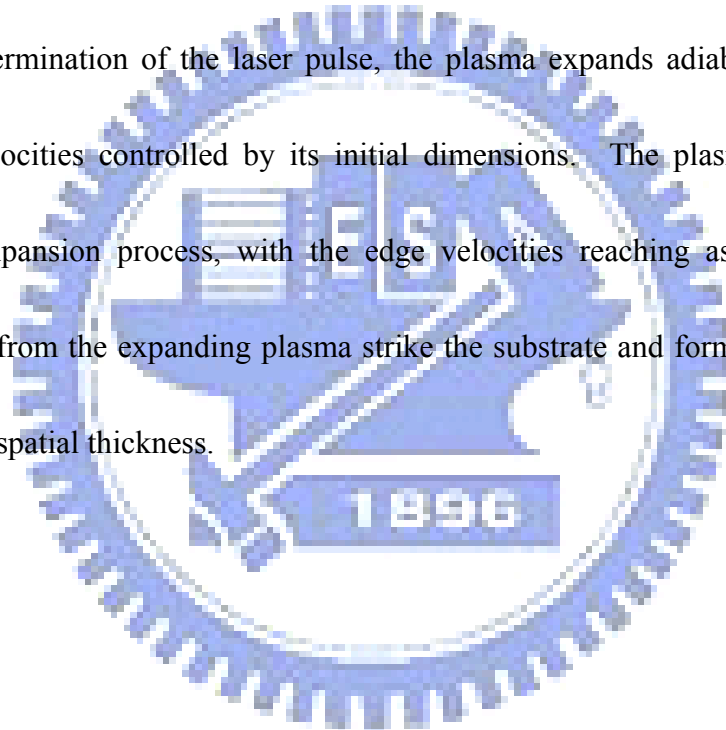
ii. Interaction of the laser beam with the evaporated material

As the evaporated material is heated by the laser beam, it results in the formation of high-temperature plasma plume consisting of ions, atoms, molecules, electrons, etc. The temperature attained by the plasma depends on the power density, frequency, pulse duration of the laser beam, and the optical and thermo physical properties of the

material. During the incidence of the laser pulse, the isothermal expanding plasma is constantly increased at its inner surface with evaporated particle from the target. The acceleration and expansion velocities in this regime are found to depend on the initial velocities of the plasma. The plasma expands preferentially normal to the irradiated surface due to the large lateral dimensions of the plasma.

iii. Adiabatic plasma expansion and deposition of thin films

After the termination of the laser pulse, the plasma expands adiabatically with the expansion velocities controlled by its initial dimensions. The plasma cools rapidly during the expansion process, with the edge velocities reaching asymptotic values. The particles from the expanding plasma strike the substrate and form a thin film with characteristic spatial thickness.



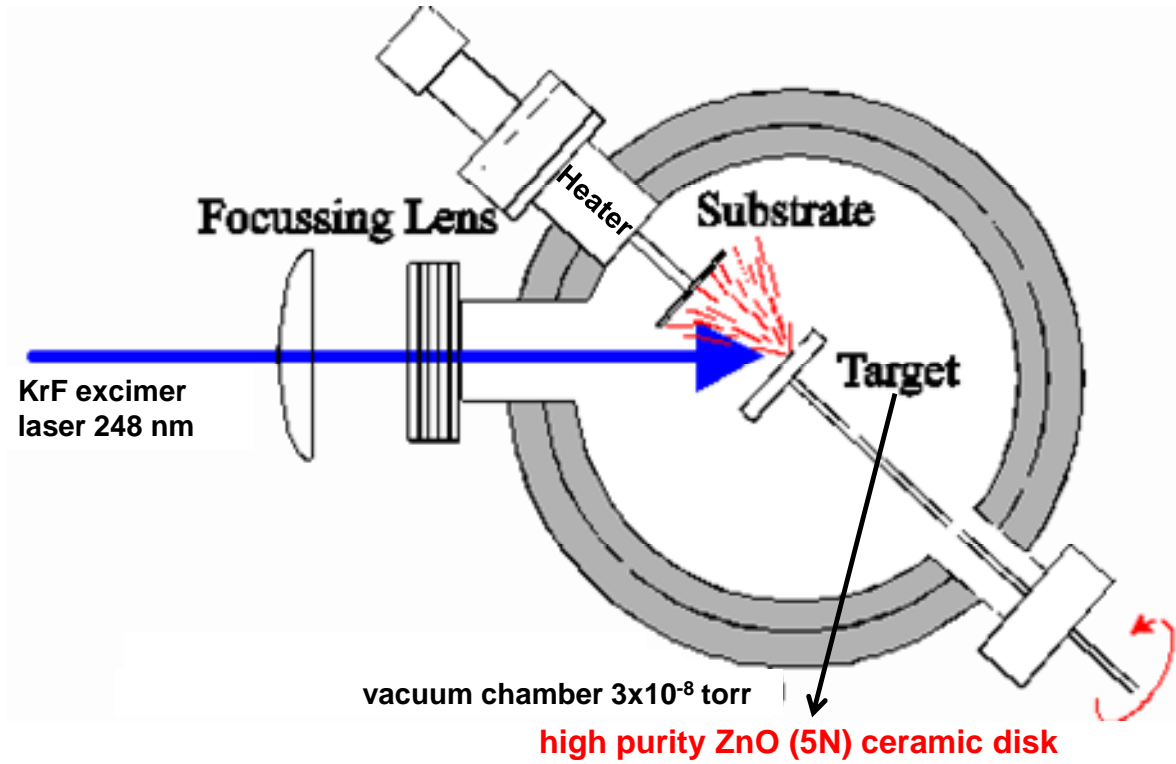


Fig. 2-1 Schematic of a laser-MBE growth system

2-2 X-ray diffraction

X-ray scattering techniques are a family of non-destructive analytical techniques which reveal information about the crystallographic structure, chemical composition, and physical properties of materials and thin films. These techniques are based on observing the scattered intensity of an x-ray beam hitting a sample as a function of incident and scattered angle, polarization, and wavelength or energy.

2-2-1 Theory of x-ray diffraction

X-ray diffraction finds the geometry or shape of a molecular. X-ray diffraction techniques are based on the elastic scattering of x-rays from structures that have long range order. A crystal consists of a regular array of atoms, each of which can scatter electromagnetic waves. A monochromatic beam of X-ray that falls on a crystal will be scattered in all directions, in certain direction the scattered waves will constructively interfere with one another while others will destructively interfere. The analysis was developed in 1913 by W. L. Bragg. The condition which must be fulfilled for radiation scattered by crystal atoms to undergo constructive interference can be obtained from a diagram like that in Fig. 2-2. In the plane wave description, a beam containing X-rays of wavelength λ impinges on a crystal at an angle θ with a family of Bragg planes, whose space is d . The beam goes past atom A in the first plane and atom B in the next, and each of them scatters part of the beam in random directions. Constructive

interference occurs only between those scattered rays whose paths differ by exactly λ , 2λ , 3λ , and so on. That is, the path difference must be $n\lambda$, where n is an integer. The only rays scattered by A and B for which this is true are those labeled I and II in Fig. 2-2. The first condition on I and II is that their common scattering angle is equal to the angle of incidence θ of the original beam. The second condition is that

$$2d\sin\theta = n\lambda, \quad n = 1, 2, 3, \dots, \quad (2-1)$$

since ray II must travel the distance $2d\sin\theta$ farther than ray I. The integer n is the order of the scattered beam. Then considering a hexagonal unit cell as shown in Fig. 2-3 which is characterized by lattice parameters a and c . The interplanar spacing d for the hexagonal structure is given as:

$$\frac{1}{d^2} = \frac{4}{3} \left[\frac{h^2 + hk + k^2}{a^2} \right] + \frac{l^2}{c^2}. \quad (2-2)$$

Combining Bragg's law with (2-2):

$$\frac{1}{d^2} = \frac{4}{3} \left[\frac{h^2 + hk + k^2}{a^2} \right] + \frac{l^2}{c^2} = \frac{4\sin^2\theta}{\lambda^2}. \quad (2-3)$$

Rearranging (2-3) gives

$$\sin^2\theta = \frac{\lambda^2}{4} \left\{ \frac{4}{3} \left[\frac{h^2 + hk + k^2}{a^2} \right] + \frac{l^2}{c^2} \right\}. \quad (2-4)$$

The lattice parameter a or c can be determined by simultaneously fitting the diffraction angles of different reflections using Eq. 2-4.

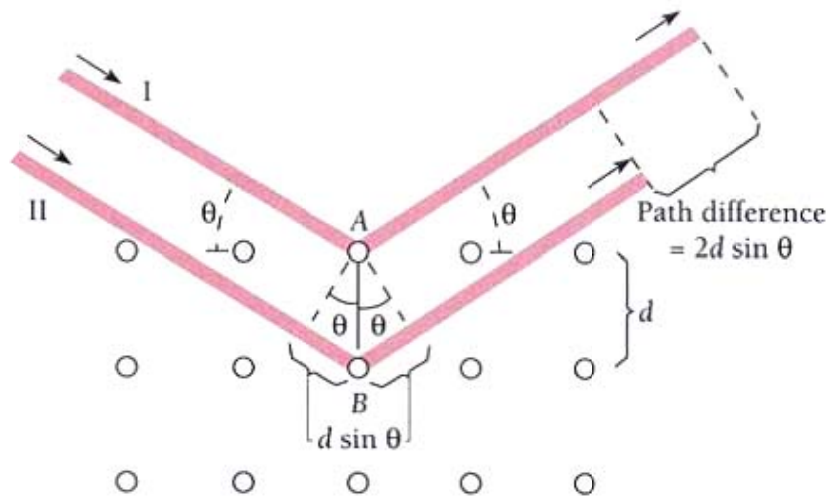


Fig. 2-2 X-ray scattering from a cubic crystal

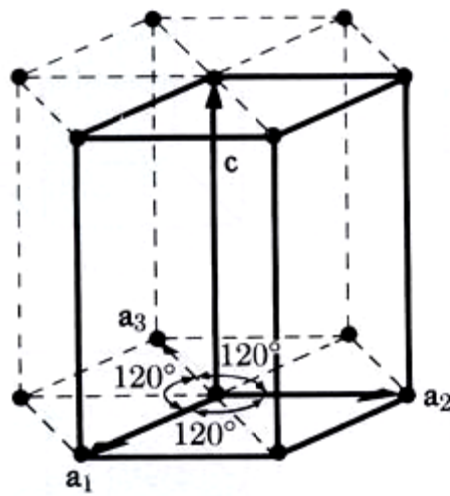


Fig. 2-3 The hexagonal unit cell

2-2-2 Rocking curve

Under a Bragg reflection condition, as shown in Fig. 2-2, crystal is rotated or called rocked through the Bragg angle θ , while the diffracted beam is measured with a fixed detector. The resultant curve of intensity vs. θ is called a rocking curve [19]. The width of a rocking curve is a direct measure of the range of orientation present in the irradiated area of the crystal because each subgrain of a typical mosaic crystal successively comes into reflecting position as the crystal is rotated [19].

2-2-3 Phi scan

Phi scan means to measure the diffraction intensity vs. azimuthal angle ϕ with rotating the crystal along the surface normal, as shown in Fig. 2-4. The intensity distribution in-plane polar angle ϕ scan can reveal the symmetry of the crystal.

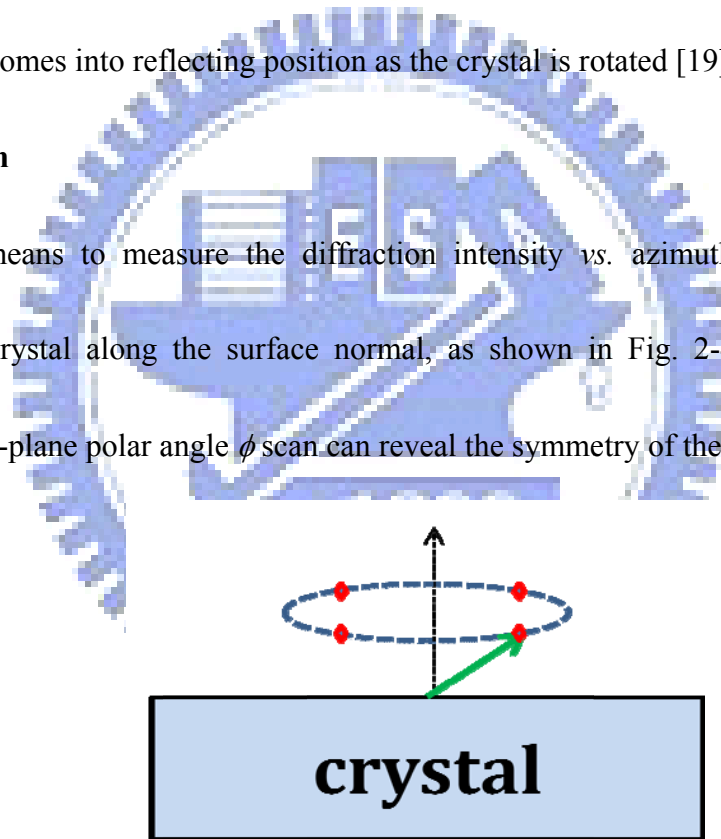


Fig. 2-4 Illustration of phi scan

2-2-4 Analysis of threading dislocation density

Figure 2-5 depicts different types of dislocations and the corresponding Burgers vectors. Before characterizing the threading dislocations (TDs), the Burgers vectors should be defined. The Burgers vector, denoted by \mathbf{b} , is a vector that represents the magnitude and direction of the lattice distortion of dislocation in a crystal lattice [20].

The magnitude and direction of vector is best understood when the dislocation-bearing crystal structure is first visualized *without* the dislocation, that is, the *perfect* crystal structure. In this perfect crystal structure, a rectangle whose lengths and widths are integer multiples of "a" (the unit cell length) is drawn *encompassing* the site of the original dislocation's origin. Once this encompassing rectangle is drawn, the dislocation can be introduced. Said rectangle could have one of its sides disjoined from the perpendicular side, severing the connection of the length and width line segments of the rectangle at one of the rectangle's corners, and displacing each line segment from each other. What was once a rectangle before the dislocation was

introduced is now an open geometric figure, whose opening defines the direction and magnitude of the Burgers vector. Specifically, the breadth of the opening defines the magnitude of the Burgers vector, and, when a set of fixed coordinates is introduced, an angle between the termini of the dislocated rectangle's length line segment and width line segment may be specified. The direction of the vector depends on the plane of

dislocation, which is usually on the closest-packed plane of unit cell. The magnitude is usually represented by equation:

$$|\mathbf{b}| = \frac{a}{2} \sqrt{h^2 + k^2 + l^2}, \text{ for a cubic system,} \quad (2-5)$$

where a is the unit cell length of the crystal, $|\mathbf{b}|$ is the magnitude of Burgers vector and h , k , and l are the components of Burgers vector, $\mathbf{b} = \langle h k l \rangle$.

TDs in a film produce crystalline plane distortions and the associated lattice deformation depends on the geometry of the TDs [21]. For a (0001) oriented thin film with wurtzite structure, the TDs are classified into three different types according to the direction of the corresponding Burgers vector (\mathbf{b}) relative to the [0001] line direction. They are edge dislocation with $\mathbf{b}_E = 1/3 \cdot \langle 11 \bar{2} 0 \rangle$, screw dislocation with $\mathbf{b}_C = \langle 0001 \rangle$, and mixed dislocation with $\mathbf{b}_M = 1/3 \cdot \langle 11 \bar{2} 3 \rangle$, which is a combination of \mathbf{b}_E and \mathbf{b}_C . For edge dislocation, the Burgers vector and dislocation line are at right angles to one another. For screw dislocation, they are parallel. Pure edge TDs twist surrounding hexagonal lattice about [0001], leading to the formation of vertical grain boundaries [22]. Under this circumstance, the $(hkil)$ crystalline planes with nonzero in-plane component, i.e. either h or k is not zero, are distorted. On the other hand, the pure screw TDs result in the tilting of the lattice, generating a pure shear strain field [23], and the crystalline planes with nonzero l are deformed. Therefore, to investigate the influence of edge TDs, measuring the profiles of $(h0\bar{h}0)$ surface reflections is

necessary, which are not sensitive to lattice distortion caused by pure screw TDs. On the other hand, measuring the line widths of the (000*l*) normal reflections, which are not affected by the pure edge TDs is a good method to characterize the screw TDs.

The broadening of radial scan line width would come from crystallite size, strain and instrument effects. The experimentally measured FWHM, B_{exp} , is a convolution of the instrumental broadening, $B_{instr.}$, and the broadening coming from the sample, of which strain induced broadening, B_{strain} , and finite crystal size induced broadening, B_{size} , are the major contributions.

As compared with the measured line width of ZnO, the instrumentation induced broadening is much smaller and thus can be safely neglected in our results. To obtain meaningful quantitative results, Williamson-Hall plot [24] is employed to analyze the quantity of domain size and strain. We make a Δq_r vs. q plot with $q = 4\pi \sin\theta/\lambda$ denoting the scattering vector and Δq_r standing for the line width in q along the radial direction to separate the broadening due to finite structural coherence length from strain induced broadening. The equation of the line in Williamson-Hall plot can be expressed as:

$$\Delta q_r = \Delta q_{size} + \Delta q_{strain} = \frac{2\pi}{L} + q\varepsilon, \quad (2-6)$$

where L and ε represent the coherent length and inhomogeneous strain, respectively.

Thus, the inverse of ordinate intercept yields the coherence length (L), i.e., the effective

domain size, and the slope yields the root-mean-square (RMS) inhomogeneous strain (ε) averaged over the effective domains [24]. The Δq_t vs. q plot, where $\Delta q_t = \Delta\theta \times q$ denoting the line width in q along the transverse direction, for θ -scans across the $(000l)$ and in-plane $(h0\bar{h}0)$ reflections, of which the slopes yield the spreads of tilt and twist angles, respectively. The density of TDs can be evaluated from the corresponding Burgers vectors and the tilt/twist angles. For screw TDs, the density N_S is calculated

according to $N_S = \frac{\alpha_\Omega^2}{4.35b_C^2}$ [25], in which α_Ω is the tilt angle and b_C denotes the length

of corresponding Burgers vector. For edge TDs, the formula employed to calculate the density, N_E , depends on the spatial arrangement of the TDs [26]. Assuming a random

distribution, we can apply $N_E = \frac{\alpha_\Phi^2}{4.35b_E^2}$, in which α_Φ stands for the twist angle. In the

case of TDs accumulating at a small-angle boundary, we should adopt the formula:

$N_E = \frac{\alpha_\Phi}{2.1|b_E|L}$, where L denotes the correlation length along the in-plane direction. In

both formulae of N_E , b_E is the length of associated Burgers vector $\mathbf{b}_E = 1/3 \langle 11\bar{2}0 \rangle$.

The real edge TDs density falls between that of random and piled up distribution.

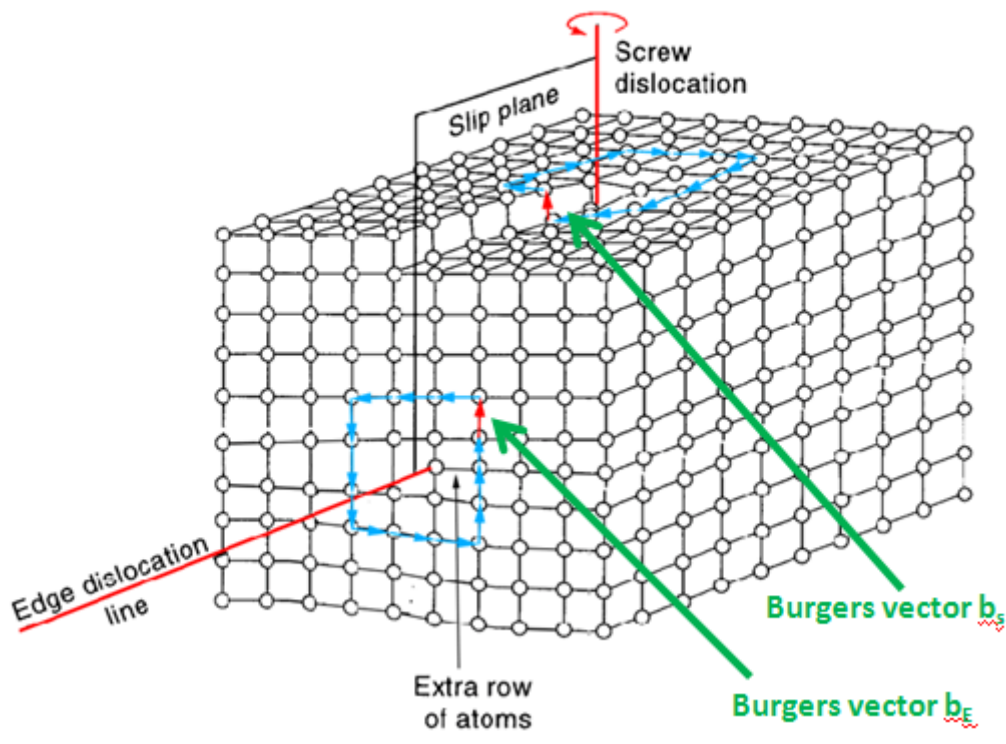


Fig. 2-5 Illustration of Burgers circuits, Burgers vectors, types of edge and screw dislocations



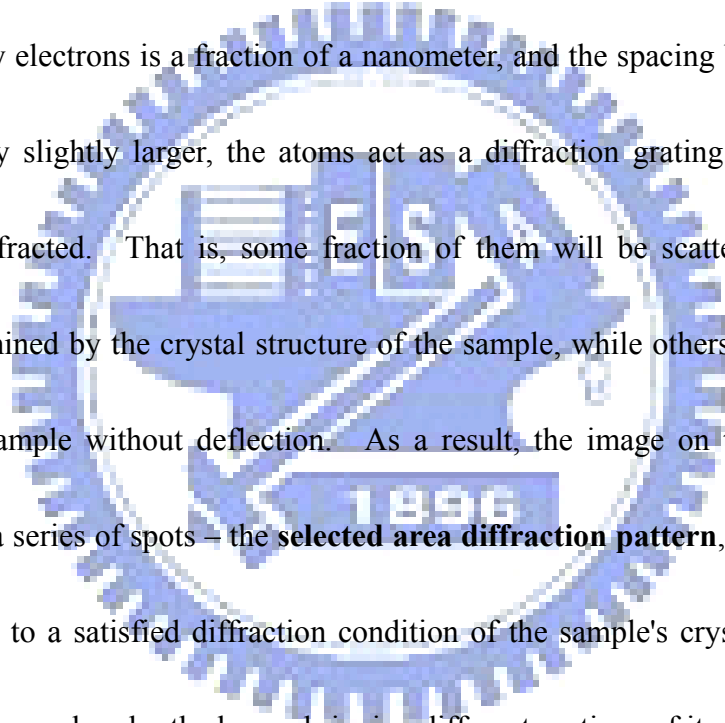
2-3 Transmission electron microscopy

The transmission electron microscope (TEM) has become the premier tool for the micro-structural characterization of materials. In practice, the diffraction patterns measured by x-ray methods are more quantitative than electron diffraction patterns, but electrons have an important advantage over x-ray- electrons can be focused easily [27].

The optics of electron microscopes can be used to make images of the electron intensity emerging from the sample. Several different techniques of TEM often employed for structural characterization are described below.

2-3-1 Selected area electron diffraction (SAED)

SAED is a crystallographic experimental technique that can be performed inside a TEM. A thin crystalline specimen is subjected to a parallel beam of high-energy electrons. The specimens are typically ~100 nm thick, and the electrons typically possess energy of 100 - 400 keV. Thus, electrons can pass through the sample easily. Electrons can be treated as wave-like, rather than particle-like. Because the wavelength of high-energy electrons is a fraction of a nanometer, and the spacing between atoms in a solid is only slightly larger, the atoms act as a diffraction grating to the electrons, which are diffracted. That is, some fraction of them will be scattered to particular angles, determined by the crystal structure of the sample, while others continue to pass through the sample without deflection. As a result, the image on the screen of the TEM will be a series of spots – the **selected area diffraction pattern**, SADP, each spot corresponding to a satisfied diffraction condition of the sample's crystal structure. If the sample is moved under the beam, bringing different sections of it under illumination, the arrangement of the spots in the diffraction pattern will change. It is useful to select a single crystal for analysis at a time. It may also be useful to select two crystals at a time, in order to examine the crystallographic orientation between them. As a diffraction technique, SADP can be used to identify crystal structures and examine crystal defects. It is similar to x-ray diffraction, but what is unique in that is area as



small as several hundred nanometers in size can be examined, whereas x-ray diffraction typically sample area several centimeters in size.

2-3-2 Analysis of threading dislocation density

The dislocation density D can be obtained by the following equation:

$$D = \frac{n}{lh}, \quad (2-7)$$

where n is obtain by counting the number n of dislocations and measuring the foil length l and foil thickness h in a cross sectional TEM image. The number of dislocations and foil length could be numbered and measured easily from the picture;

however, the foil thickness has to be derived from thickness fringe in TEM image.

From the Howie-Whelan equations, the intensity of Bragg diffracted beam can be written as [28]:

$$I_g = |\varphi_g|^2 = \left(\frac{\pi t}{\xi_g}\right)^2 \left(\frac{\sin^2(\pi t s_{eff})}{(\pi t s_{eff})^2}\right) = 1 - I_0, \quad (2-8)$$

where t is the z axial distance of intensity at the bottom of the specimen, I_g is the dark field image intensity, φ_g is the amplitude of the diffracted beam for reflection G, s_{eff} is

the effective excitation error

$$s_{eff} = \sqrt{s^2 + \frac{1}{(\xi_g)^2}}, \quad (2-9)$$

with s being a measure of how far deviating from the exact Bragg condition, and the excitation ξ_g being the characteristic length distance for the diffraction vector \mathbf{g} and

also named as extinction distance. The extinction distance can be described as:

$$\xi_g = \frac{\pi V_c \cos \theta_B}{\lambda F_g}, \quad (2-10)$$

where λ is the wavelength of electrons, F_g is the structure factor for the diffraction vector \mathbf{g} , V_c is the volume of a unit cell and θ_B is Bragg angle. If we neglect the relativistic effects:

$$\frac{1}{2} m_0 v^2 = eE, v = \sqrt{\frac{2eE}{m_0}}, \quad (2-11)$$

$$p = m_0 v = \sqrt{2m_0 eE}, \quad (2-12)$$

$$\lambda_0 = \frac{h}{p} = \frac{h}{\sqrt{2m_0 eE}}, \quad (2-13)$$

If take relativistic effects into account:

$$m c^2 = m_0 c^2 + eE, m^2 c^4 = m_0^2 c^4 + 2m_0 c^2 eE + e^2 E^2, \quad (2-14)$$

$$m = \frac{m_0}{\sqrt{1 - \frac{v^2}{c^2}}}, m^2 \left(1 - \frac{v^2}{c^2}\right) = m_0^2, m^2 c^2 = m^2 v^2 + m_0^2 c^2. \quad (2-15)$$

Combining (2-12) into (2-15) gives:

$$m^2 c^2 = p^2 + m_0^2 c^2, m^2 c^4 = p^2 c^2 + m_0^2 c^4; \quad (2-16)$$

Combining (2-14) into (2-16) gives:

$$p^2 c^2 = 2m_0 c^2 eE + e^2 E^2, p^2 = 2m_0 eE + \frac{e^2 E^2}{c^2}; \quad (2-17)$$

And combining (2-17) into (2-13) gives:

$$\lambda = \frac{h}{p} = \frac{1}{\sqrt{2m_0 eE + \frac{e^2 E^2}{c^2}}} = \frac{h}{\sqrt{2m_0 eE} \sqrt{1 + \frac{eE}{2m_0 c^2}}} = \frac{\lambda_0}{\sqrt{1 + \frac{eE}{2m_0 c^2}}}, \quad (2-18)$$

where h is the Plank's constant equal to 6.626×10^{-34} Nms, p is the momentum of electron, charge e equals to -1.602×10^{-19} C, rest mass $m_0 = 9.109 \times 10^{-31}$ kg, speed of light in vacuum $c = 2.998 \times 10^9$ m/sec.

For acceleration voltage 200 kV, the relativistic wavelength is 0.0251 Å. For hexagonal ZnO operated at 200 keV, $\mathbf{g} = (0002)$, $a = 3.2438$ Å and $c = 5.2036$ Å, Eq. (2-4) gives $\theta_B = 0.27689^\circ$, where θ_B is Bragg angle. The structure factor F_g of ZnO with diffraction vector $\mathbf{g} = (0002)$ is $F_{0002} = 11.564$ Å and the volume of a unit cell $V_c = \frac{a^2 c \sqrt{3}}{2} = 47.6199$ Å³. Substituting these parameters into Eq. (2-10) gives $\xi_g = \frac{\pi V_c \cos \theta_B}{\lambda F_g} = 515.4$ Å. Considering Eq. (2-8) for only one diffraction beam \mathbf{g} , the two-beam approximation is applied. The two-beam condition means that we tilt the crystal so that there are only two strong beams exist. One is the direct beam and the other is the diffraction beam with $s = 0$. The rest of the diffracted beams are very weak ($s \gg 0$ or $\ll 0$) and the contribution to φ_g is ignored. Then, Eq. (2-9) becomes $s_{eff} = \frac{1}{\xi_g}$. Simplify Eq. (2-8), we have $I_g = |\varphi_g|^2 = \sin^2\left(\frac{\pi t}{\xi_g}\right) = 1 - I_0$, for $t = 0$ or $t = n\xi_g$, $I_g = 0$ and for $t = \frac{1}{2}\xi_g$, $I_g = 1$. The oscillatory intensity variations with t are illustrated in Fig. 2-6.

For hexagonal ZnO with two-beam condition $\mathbf{g} = (0002)$, $t = \frac{1}{2}\xi_{0002} = 257.7$ Å for the first dark fringe. With given foil thickness, the dislocation density can be evaluated from the Eq. (2-7).

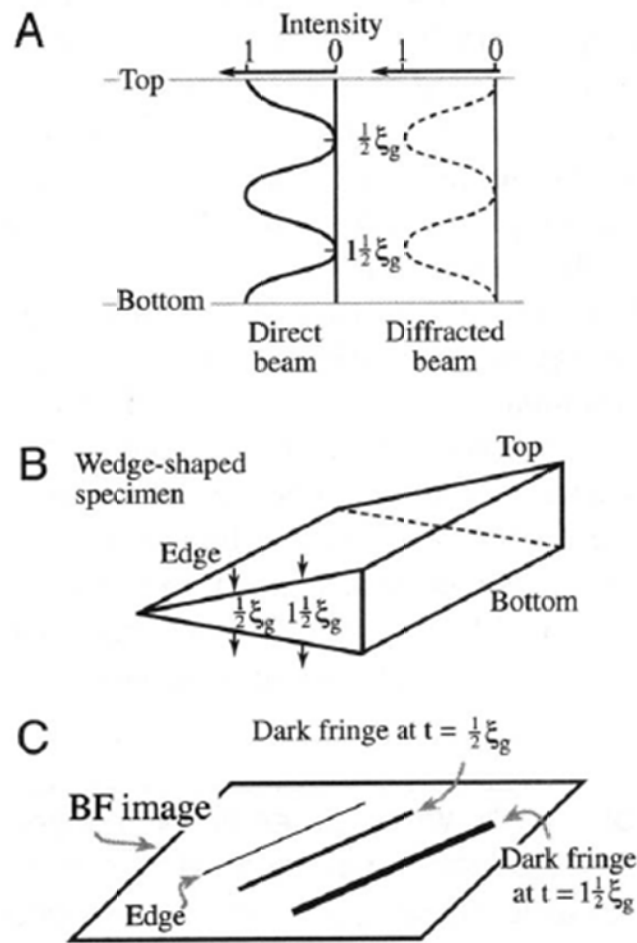


Fig. 2-6 The TEM image contrast of a wedge-shaped specimen. At the Bragg condition ($s = 0$), the intensities of the direct and diffracted beams oscillate in a complementary way (A). For a wedge specimen, shown in (B), the separation of the fringes in the image, shown in (C) is determined by the angle of the wedge and the extinction distance, ξ_g .

2-4 Photoluminescence characterization

PL is a very useful and powerful optical characterization tool in the semiconductor industry, with its sensitive ability to reveal the emission mechanism and band structure of semiconductors. From PL spectra the defects or impurities can also be identified in the compound semiconductors, which affect material quality and device performance. A given impurity produces a set of characteristic spectral features. The fingerprint can be used to identify the impurity type. Often several different impurities can be found in a single PL spectrum. In addition, the line width of each PL peak is an indication of sample's quality, although such analysis has not yet become highly quantitative.

PL is the optical radiation emitted by a physical system (in excess the thermal equilibrium blackbody radiation) resulting from excitation to a non-equilibrium state by irradiation with light. Three processes can be distinguished: (i) creation of electron-hole pairs by absorption of the incoming light, (ii) radiative recombination of electron-hole pairs, and (iii) escape of the recombination radiation from the sample.

Since the incoming light is absorbed to create electron-hole pairs, the greatest excitation of the sample occurs near the surface; the resulting carrier distribution is both inhomogeneous and non-equilibrium. In attempting to regain homogeneity and equilibrium, the excess carriers will diffuse away from the surface while being depleted by both radiative and nonradiative recombination processes. Most of the excitation of

the crystal is thereby restricted to a region within a diffusion length (or absorption length) of the illuminated surface. Consequently, the vast majority of PL experiments are arranged to examine the light emitted from the irradiated side of the samples. This is often called front surface PL.

2-4-1 Fundamental Transitions

Since emission requires the system being in a non-equilibrium condition, some means of exciting energy is acting on the semiconductor to produce hole-electron pairs. We summarize the fundamental transitions, those occurring at or near the band edges as below.

1. Free excitons

A free hole and a free electron as a pair of opposite charges experience a coulomb attraction. Hence the electron can orbit about the hole as a hydrogen-like atom. If the material is sufficiently pure, the electrons and holes pair into excitons which then recombine, emitting a narrow spectral line. In a direct-gap semiconductor, where momentum is conserved in a simple radiative transition, the energy of the emitted photon is simply

$$h\nu = E_g - E_x,$$

where E_g and E_x are the band gap and the exciton binding energy.

2. Bound excitons

Similar to the way that free carriers can be bound to (point-) defects, it is found that excitons can also be bound to defects. A free hole can combine with a neutral donor to form a positively charged excitonic ion. In this case, the electron bound to the donor still travels in a wide orbit about the donor. The associated hole, which moves in the electrostatic field of the “fixed” dipole, determined by the instantaneous position of the electron, also travels about this donor; for this reason, this complex is called a “bound exciton”. An electron associated with a neutral acceptor is also a bound exciton. The binding energy of an exciton to a neutral donor (acceptor) is usually much smaller than the binding energy of an electron (hole) to the donor (acceptor).

3. Donor-Acceptor Pairs

Donors and acceptors can form pairs and act as stationary molecules imbedded in the host crystal. The coulomb interaction between a donor and an acceptor results in a lowering of their binding energies. In the donor-acceptor pair case it is convenient to consider only the separation between the donor and the acceptor level:

$$E_{pair} = E_g - (E_D - E_A) + \frac{q^2}{\epsilon r} ,$$

where r is the separation of donor-acceptor pair, E_D and E_A are the respective ionization energies of the donor and the acceptor as isolated impurities.

4. Deep transitions

By deep transition we shall mean either the transition of an electron from the

conduction band to an acceptor state or a transition from a donor to the valence band in Fig. 2-7. Such a transition emit a photon $h\nu = E_g - E_i$ (E_i stands for E_D or E_A) for direct transitions and $h\nu = E_g - E_i - E_p$ if the transition is indirect and involves a phonon of energy E_p . Hence the deep transitions can be distinguished as (1) conduction-band-to-acceptor transition which produces an emission peak at $h\nu = E_g - E_A$, and (2) donor-to-valence-band transition which produces an emission peak at the higher photon energy $h\nu = E_g - E_D$.

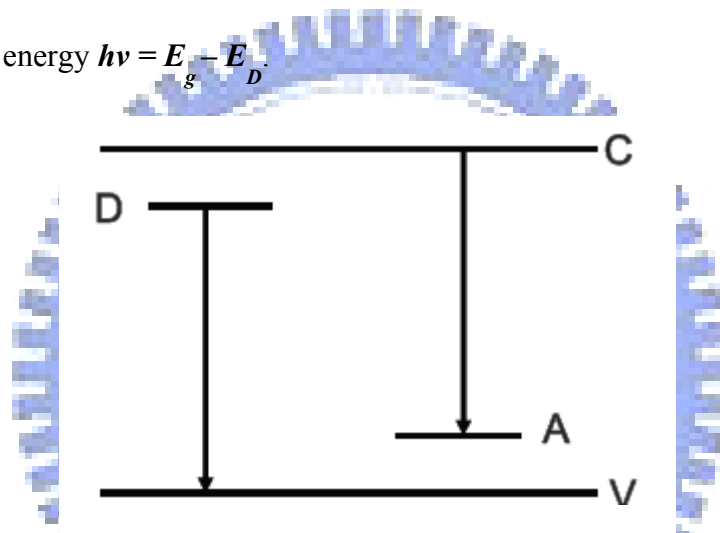


Fig. 2-7 Radiative transitions between a band and an impurity state

5. Transitions to deep levels

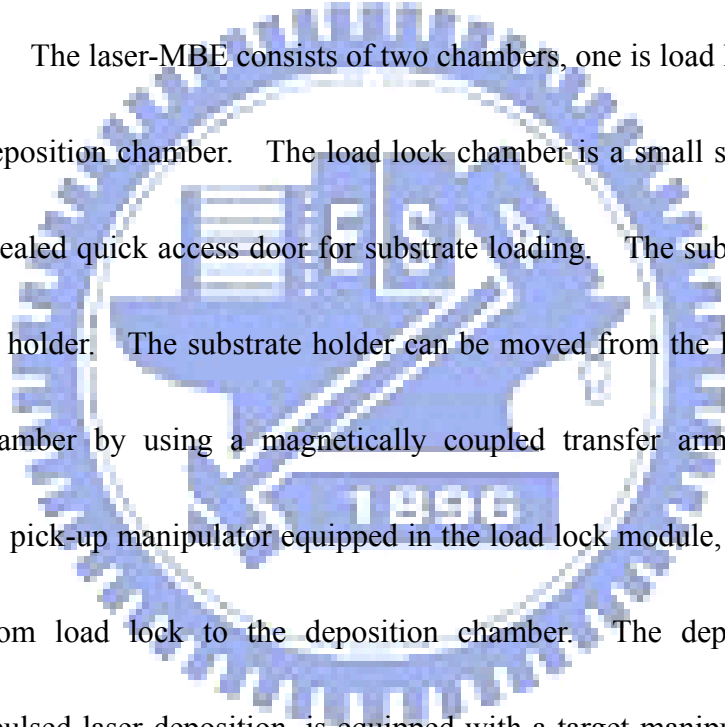
Some impurities have large ionization energies; therefore, they form deep levels in the energy gap. Radiative transitions between these states and the band edge emit at $h\nu = E_g - E_i$. Some defects not only (or a few) levels close to one band, but have several of levels partly around the middle of the gap. They give rise to the green, orange and red emission bands of wide-gap semiconductor such as ZnO and ZnS.

Chapter 3 Experimental details

3-1 The growth of ZnO films

3-1-1 Description of Laser-MBE system

The laser-molecular beam epitaxy (laser-MBE) growth system is also known as pulsed-laser deposition (PLD) and has been used to grow high quality films for more than a decade. The laser-MBE consists of two chambers, one is load lock chamber and the other is deposition chamber. The load lock chamber is a small spherical chamber with a Viton sealed quick access door for substrate loading. The substrate is mounted on a substrate holder. The substrate holder can be moved from the load lock into the deposition chamber by using a magnetically coupled transfer arm. By using the push-pull type pick-up manipulator equipped in the load lock module, substrates can be transferred from load lock to the deposition chamber. The deposition chamber, designed for pulsed laser deposition, is equipped with a target manipulator, a substrate holding and heating system, a pumping system, vacuum monitoring devices, necessary parts for laser inlet and a watching window.



3-1-2 The layout of laser-MBE system

The laser-MBE growth system consists of two chambers, the load lock chamber and the growth chamber, as shown in Fig. 3-1. There is a gate valve between two chambers. A combination of scroll pump and turbo pump is used to achieve high vacuum pressure ($< 10^{-8}$ torr).

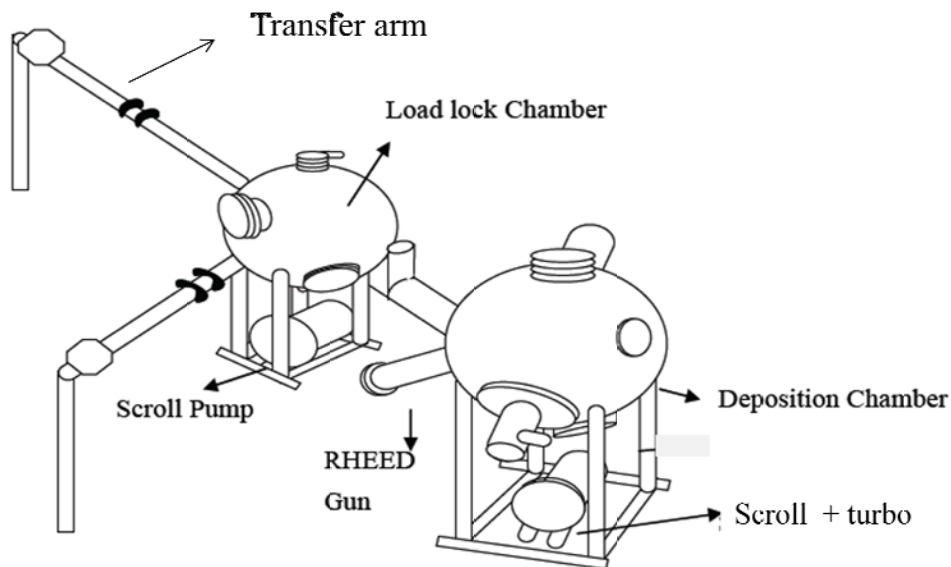


Fig. 3-1 Layout of laser-MBE system

The ZnO thin films were prepared by the Laser-MBE deposition utilizing a KrF pulsed excimer laser (Lambda Physics LPX 210i). The detailed data sheet of KrF laser is shown below.

Table 3-1 LPX210i (KrF) Specifications

Wavelength	Pulse Energy	Max. Rep. Rate	Average Power	Pulse Duration	Beam Dimension	Beam Divergence
248 nm	700 mJ	100 HZ	65 W	25 ns FWHM	5-12x23 mm²	1 x 3 mrad

3-1-3 Target preparation

The target was prepared by commercial hot-pressed stoichiometric ZnO target with purity of 99.999% and the target size is 1" × 0.118". Before the deposition, the laser beam was shone on the ZnO target to remove the contamination on the target surface.

3-1-4 Preparation of substrate

The composite γ -Al₂O₃/Si substrate was prepared by advanced nano epitaxy laboratory, NTHU, led by Prof. M. Hong and Prof. J. Kwo. The detailed preparation procedure of the substrate can be found in [29] and is also briefly described below.

Si wafers 2 inch in diameter with (111) as the normal to the wafer plane were put into a multi-chamber MBE/ultrahigh vacuum (UHV) system [30], after being cleaned with a Radio Corporation of America (RCA) method and an HF dip. Si wafers were heated to temperatures above ~550 °C, and then transferred under an UHV (to eliminate any possibility of Si oxidation), to an oxide growth chamber for the Al₂O₃ deposition. A

high-purity sapphire (purchased from Maintech, Huntingdon, PA, with a purity of 99.99%) was employed as the Al_2O_3 source in this work. During the oxide deposition, the vacuum in the chamber was maintained in the low 10^{-9} torr (even during the evaporation of sapphire) and substrate temperatures were maintained at about 700–750 °C. After the deposition of Al_2O_3 , the substrates ($\gamma\text{-Al}_2\text{O}_3/\text{Si}$) were cut into pieces of an area of $1 \times 1 \text{ cm}^2$ for subsequent epitaxial growth of ZnO. Before transferring these substrates into laser-MBE load lock chamber, each substrate was put in acetone solution and cleaned in a supersonic oscillator for 5 minutes to remove the particles on the substrate surface. After the surface treatment, the substrates were mounted on the substrate holder and loaded into the ZnO growth chamber.

3-1-5 Operating process of laser-MBE

- (1) Load the mounted substrate holder into the load lock chamber and turn on the scroll pump.
- (2) After the pressure of the chamber is pumped down to lower than 3×10^{-3} torr, then turn the turbo pump on.
- (3) The pressure of the chamber should reach 10^{-9} torr in three hours. Only at this condition, we open the gate valve between the load lock and deposition chamber.

We use the magnetically coupled transfer arm to transfer the substrate holder from the load lock chamber into the deposition chamber.

- (4) After substrate transferred, close the gate valve.
- (5) Adjust the distance between the substrate and ZnO target to reach the appropriate position.
- (6) Make sure the water cooling system works properly.
- (7) Turn on the thermal controller and power supply. Set the desired thermal program.
- (8) Ensure the target substrate temperature is reached. Wait for a few minutes to let the chamber pressure decline to 3×10^{-8} .
- (9) Turn on step motor to start the mirror scanner. Turn on target manipulator and sample manipulator rotation to ensure the uniformed deposition.
- (10) Turn on the laser and start the deposition.
- (11) After thin film growth is completed, open the gate valve and use the magnetically coupled transfer arm to retrieve the sample from the main chamber to the load lock chamber.
- (12) Stop the turbo and scroll pump. When the blades of the turbo pump stop, we can vent the load lock chamber by inserting N_2 gas.

After surface treatment, the substrate was loaded in the chamber with the base pressure of 1×10^{-9} torr. We used a focused lens ($f = 40$ cm) to converge the laser beam through a viewpoint onto the target, which makes 45 degrees to the normal of the target. Inside the growth chamber, a ZnO ceramic target (99.999 % purity) was

located in front of the substrate holder at a distance of 5 cm and was ablated by a KrF excimer pulsed-laser with the wavelength, pulse duration, repetition rate, and laser fluence of 248 nm, 25 ns, 10 Hz, and 6 J/cm², respectively. At the same time, the laser beam was scanned back and forth by moving a reflection mirror, which was driven by a stepping motor to prevent laser from hitting at the same spot on the target that leads to penetrate the target or non-uniform film growth. The substrate was heated with a halogen light bulb through the program temperature controller. The temperatures of the substrate holder were varied from 200°C to 500°C. The deposition of the ZnO thin films was carried out without oxygen flowing, under this circumstances, the pressure was maintained at 1×10^{-9} torr during deposition. The typical growth rate and sample thickness were 0.42 Å/s and ~300 nm, respectively.

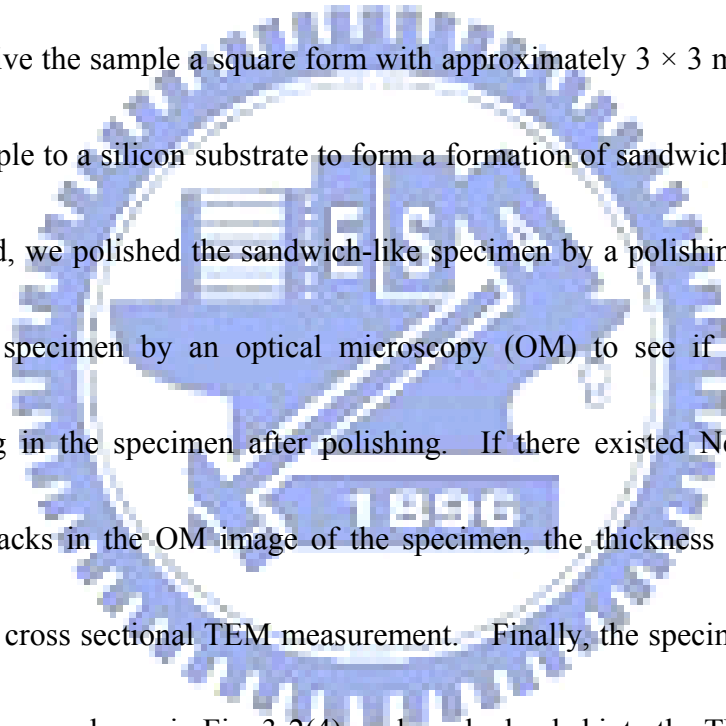
3-2 Structural characterization of the ZnO films

3-2-1 X-ray diffraction

The crystal structure of ZnO films was inspected by XRD measurements which were performed with a four-circle diffractometer at the beamlines BL17A and BL13A of National Synchrotron Radiation Research Center, Taiwan, with incident wavelength 1.3344 and 1.023 Å, respectively. Two pairs of slits, located between the sample and a NaI scintillation detector, were employed and yielded a typical resolution of 4×10^{-3} Å⁻¹.

3-2-2 Cross sectional TEM

Cross sectional TEM images and SAED patterns were taken using a field-emission-gun type TEM (Philips TECNAI-20) operated at 200 keV. For the preparation of cross-sectional TEM specimens, several steps of lapping and polishing are required. Figures 3.2(1) – (4) shows the specimen preparation processes. The first step of the preparation was a mechanical treatment of the materials, like sawing or punching to give the sample a square form with approximately 3×3 mm. Second, we glued the sample to a silicon substrate to form a formation of sandwich, as show in Fig. 3-2(2). Third, we polished the sandwich-like specimen by a polishing machine. We observed the specimen by an optical microscopy (OM) to see if there occurred a Newton's ring in the specimen after polishing. If there existed Newton's ring and showed no cracks in the OM image of the specimen, the thickness of specimen was proper for the cross sectional TEM measurement. Finally, the specimen was mounted on a copper ring, as shown in Fig. 3-2(4), and can be loaded into the TEM measurement holder.



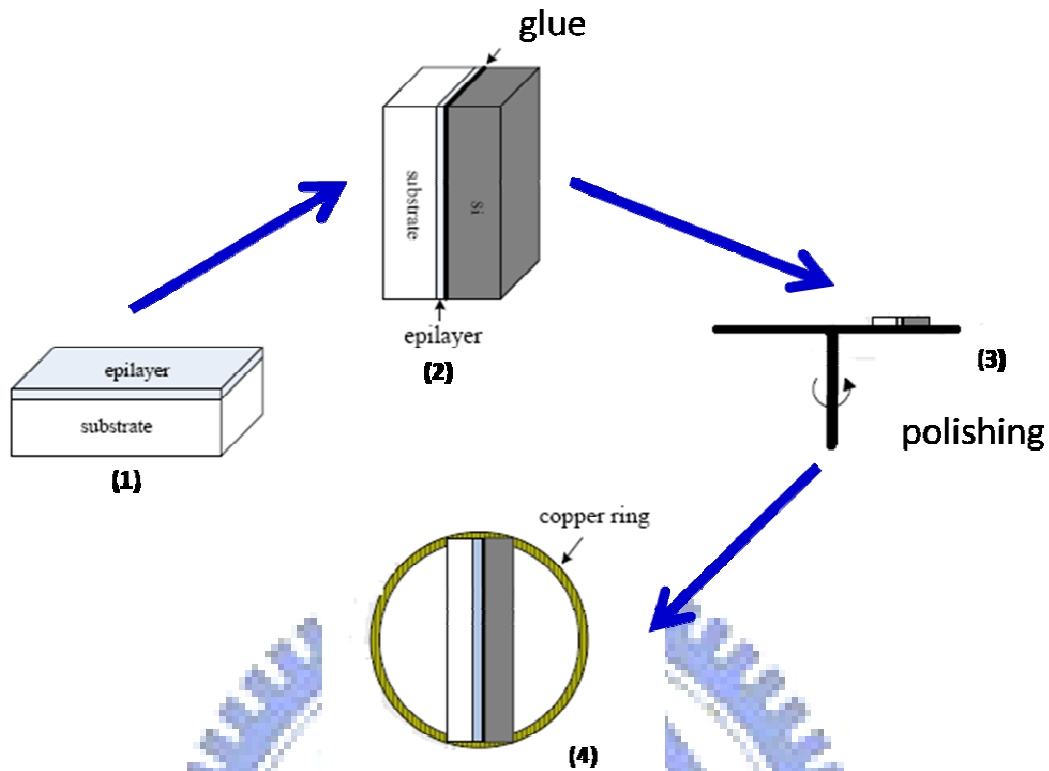


Fig. 3-2 A schematic showing the preparation of a cross-sectional TEM specimen

3-3 Measurements of optical properties

3-3-1 Photoluminescence detection system

A He-Cd laser (Kimmon IK5552R-F) operating at 325 nm UV line is commonly utilized as a pumping source for PL. Figure 3-2 depicts the PL system setup including reflection mirrors, focusing and collecting lens, sample holder and cooling system.

We utilized two single-grating monochromators (Triax 320) equipped with a photo-multiplier tube (PMT) which is matched with a photon counter for detection.

The normal operating voltage of PMT is 0.8 kV. Moreover, we used fluorescent lamps

to calibrate spectral response of the spectrometer and detector. Each PL signal was collected for about 0.1 second at a step of 0.1 nm, and the data were transmitted through a GPIB card and recorded by a computer. The monochromator was a 32 cm long with three available resolutions of lines 600, 1200 and 1800 grooves/mm, respectively. When the entrance and exit slits were both opened at about 50 μm , the resolution was about 0.1 nm in this system. Low temperature PL measurements were carried out by collecting the sample using a closed cycle cryogenic system.

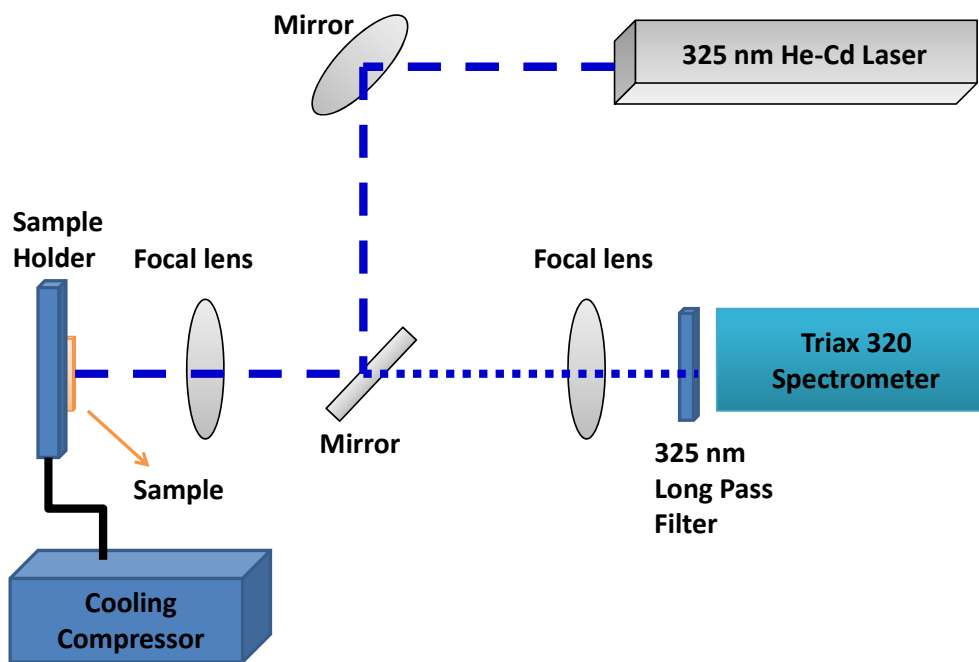


Fig. 3-3 Layout of PL system

Chapter 4 Results and Discussion

4-1 Results of X-ray measurements

4-1-1 Growth temperature dependent crystallinity of the ZnO films

ZnO films were deposited at a substrate temperature ranging from 200 to 500°C.

Two batches of samples were grown on two composite substrates, which were prepared nominally under the same deposition conditions.

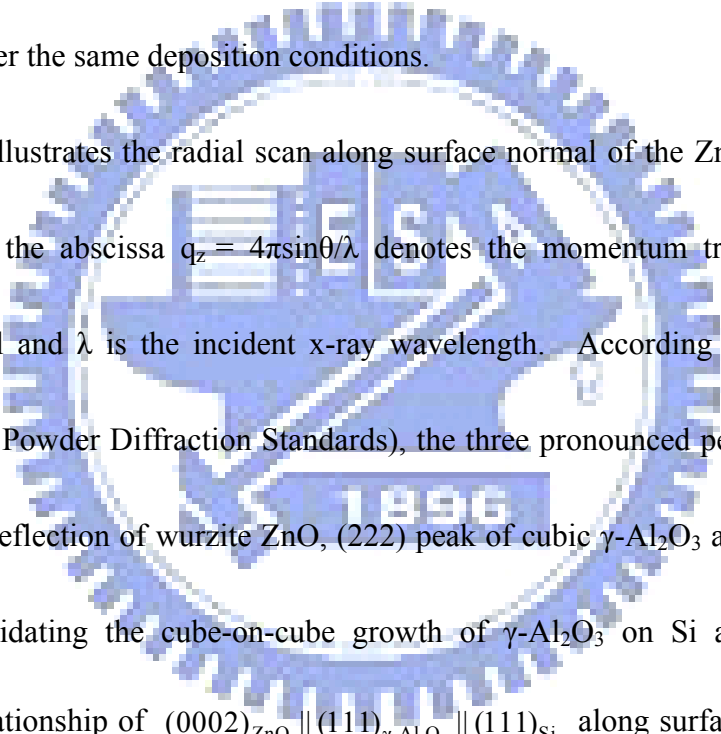
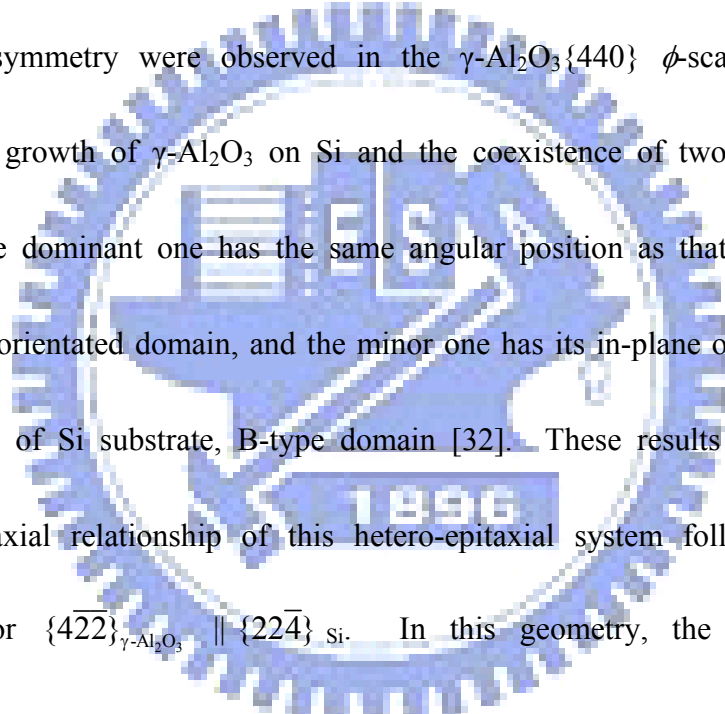


Figure 4-1 illustrates the radial scan along surface normal of the ZnO film grown at 300°C, where the abscissa $q_z = 4\pi\sin\theta/\lambda$ denotes the momentum transfer along the surface normal and λ is the incident x-ray wavelength. According to JCPDS (Joint Committee on Powder Diffraction Standards), the three pronounced peaks are assigned as the (0002) reflection of wurzite ZnO, (222) peak of cubic γ -Al₂O₃ and (111) peak of cubic Si, elucidating the cube-on-cube growth of γ -Al₂O₃ on Si and a crystalline orientation relationship of $(0002)_{\text{ZnO}} \parallel (111)_{\gamma\text{-Al}_2\text{O}_3} \parallel (111)_{\text{Si}}$ along surface normal. The pronounced thickness fringes observed near the γ -Al₂O₃(222) reflection indicates the sharpness of the γ -Al₂O₃ interfaces; the fringe period yields a layer thickness of ~15.3 nm. From the FWHM of the γ -Al₂O₃(222) reflection, we derived the vertical coherence length of the buffer layer, using the Scherrer's equation, to be ~15 nm, which is close to the layer thickness. This implies that the structural coherence of the buffer

layer is maintained over almost the entire layer thickness.

Azimuthal cone scans (ϕ -scans) across the off-normal ZnO $\{10\bar{1}0\}$, γ -Al₂O₃ $\{440\}$, and Si $\{220\}$ reflections, as shown in Fig. 4-2, were measured to examine their in-plane epitaxial relationship. Six ZnO diffracted peaks evenly spaced 60° apart confirmed that ZnO film with a six-fold rotational symmetry against surface normal was grown epitaxially on the γ -Al₂O₃/Si(111) composite substrate. Furthermore, two sets of peaks with 3-fold symmetry were observed in the γ -Al₂O₃ $\{440\}$ ϕ -scan, revealing the cube-on-cube growth of γ -Al₂O₃ on Si and the coexistence of two in-plane rotated variants. The dominant one has the same angular position as that of the Si $\{220\}$, A-type (111) orientated domain, and the minor one has its in-plane orientation rotated 60° from that of Si substrate, B-type domain [32]. These results suggest that the in-plane epitaxial relationship of this hetero-epitaxial system follows $\{10\bar{1}0\}_{\text{ZnO}} \parallel \{22\bar{4}\}_{\gamma\text{-Al}_2\text{O}_3}$ or $\{4\bar{2}2\}_{\gamma\text{-Al}_2\text{O}_3} \parallel \{22\bar{4}\}_{\text{Si}}$. In this geometry, the two-dimensional hexagonal unit cell of the γ -Al₂O₃(111) plane is aligned with the ZnO basal plane having its lattice constant equal to $\sqrt{2} \cdot a(\gamma\text{-Al}_2\text{O}_3) = 11.186 \text{ \AA}$, about 3.45 times larger than that of ZnO.



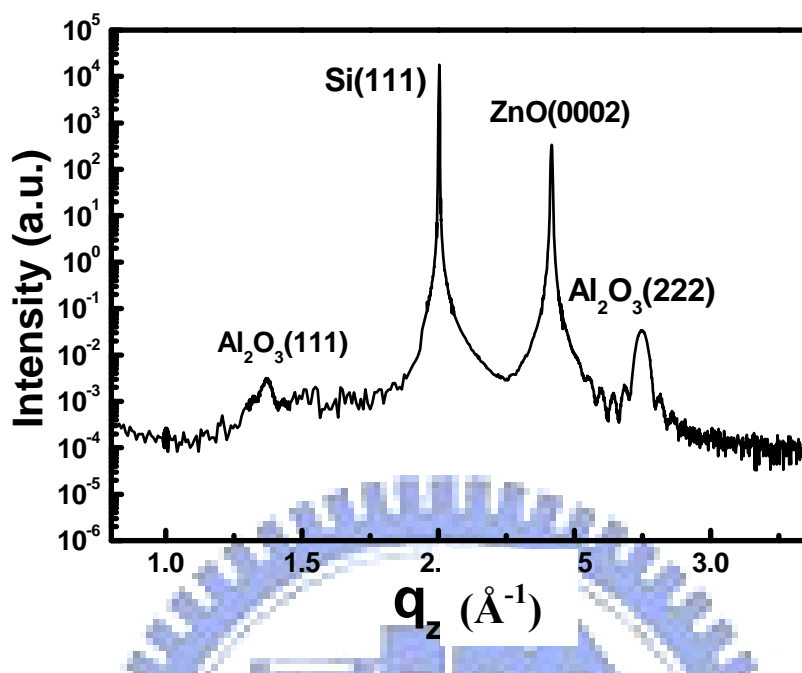


Fig. 4-1 Radial scan along the surface normal of a 300 nm thick ZnO layer grown on γ - Al_2O_3 /Si(111) composite substrate

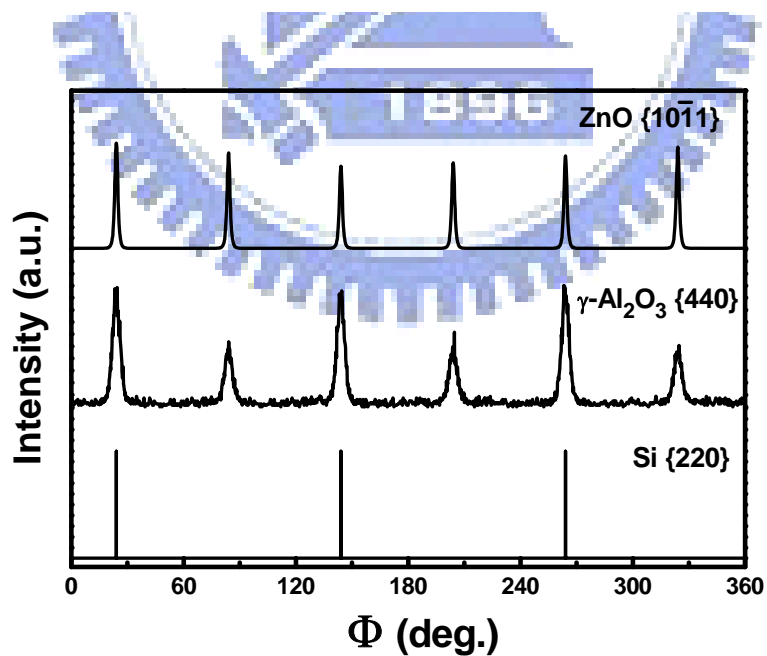
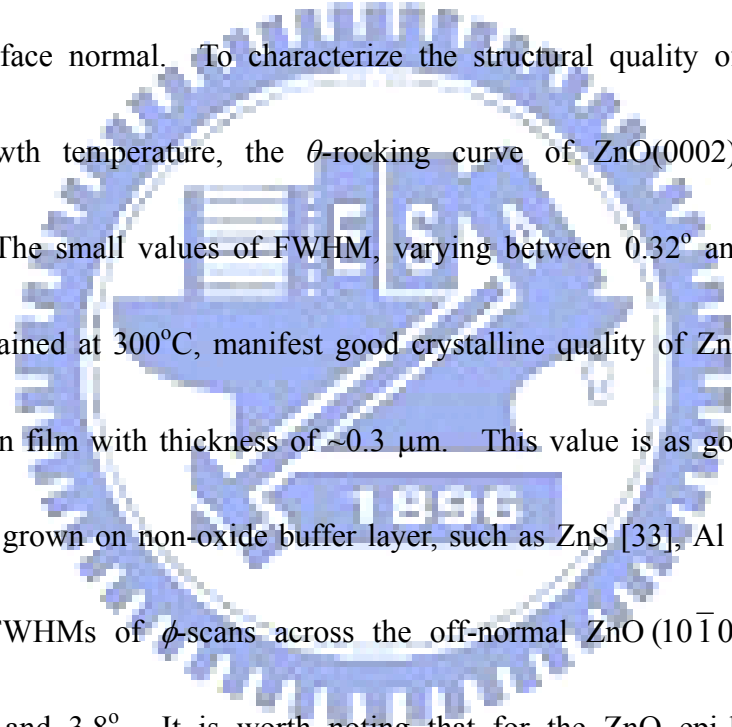
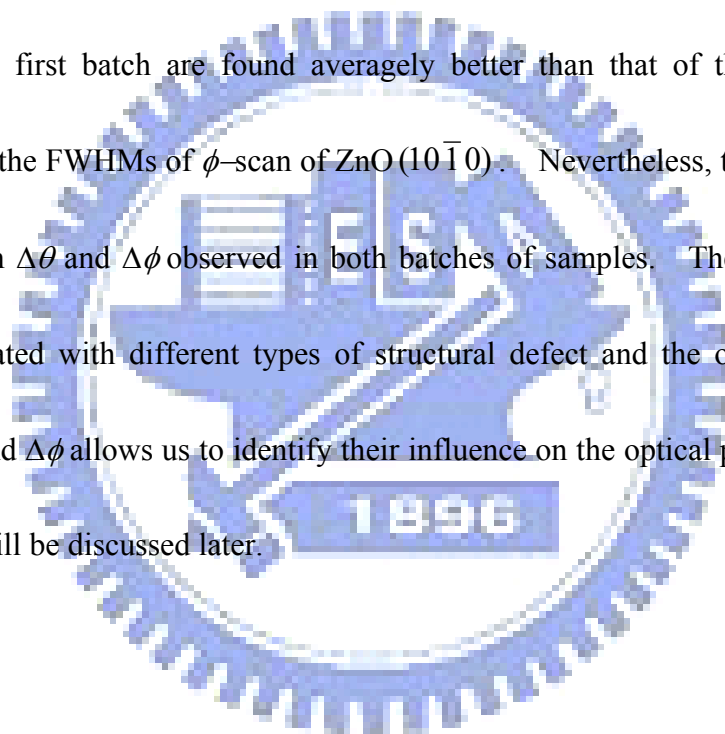


Fig. 4-2 The profile of ϕ -scans across ZnO $\{10\bar{1}0\}$, γ - Al_2O_3 (440) and Si $\{220\}$ reflections

Within the employed growth temperatures, all the samples exhibit the same structural characteristics with a small variation of less than 0.2% in ZnO lattice parameters. The lattice parameters of ZnO bulk are $a = 3.2438 \text{ \AA}$ and $c = 5.2036 \text{ \AA}$, derived from the XRD data of a ZnO wafer. As compared with the lattice parameters of the grown ZnO films, we found that all the ZnO films experience a tensile strain ($\sim 0.28\%$) in the lateral direction and correspondingly a compressive strain ($\sim 0.19\%$) along the surface normal. To characterize the structural quality of the film under different growth temperature, the θ -rocking curve of ZnO(0002) reflection was performed. The small values of FWHM, varying between 0.32° and 0.61° with the minimum obtained at 300°C , manifest good crystalline quality of ZnO epi-layer even for such a thin film with thickness of $\sim 0.3 \mu\text{m}$. This value is as good as that of the ZnO epi-film grown on non-oxide buffer layer, such as ZnS [33], Al [34] and 3C-SiC [35]. The FWHMs of ϕ -scans across the off-normal ZnO(10 $\bar{1}$ 0) reflection fall between 1.4° and 3.8° . It is worth noting that for the ZnO epi-layers grown on $\gamma\text{-Al}_2\text{O}_3/\text{Si}(111)$ under different growth temperatures, those have smaller FWHM of (0002) θ -rocking curve always have larger width in ϕ -scans across the off-normal (10 $\bar{1}$ 0) reflection, as shown in Fig. 4-3(a) and (b). This is different from ZnO grown on other substrates, such as c-plane sapphire, where both FWHMs always exhibit the same trend of increase/decrease with growth conditions [36]. Furthermore, we grew



ZnO film on two batches of buffer layers and found the structural quality of ZnO is sensitive to the structural perfection of γ -Al₂O₃ buffer layer. The FWHM of θ -rocking curve of γ -Al₂O₃(222) of the first and the second batches are 0.023° and 0.024°, respectively, while the FWHM of ϕ -scan across the off-normal γ -Al₂O₃(440) reflection are 3.97° and 4.27° for the first and the second batches, respectively. The quality of buffer layer of the first batch is better than that of the second batch. The ZnO films grown on the first batch are found averagely better than that of the second batch, especially for the FWHMs of ϕ -scan of ZnO(10 $\bar{1}$ 0). Nevertheless, the opposite trend of variation in $\Delta\theta$ and $\Delta\phi$ observed in both batches of samples. The factors, $\Delta\theta$ and $\Delta\phi$ are associated with different types of structural defect and the opposite variation trend of $\Delta\theta$ and $\Delta\phi$ allows us to identify their influence on the optical properties of ZnO film, which will be discussed later.



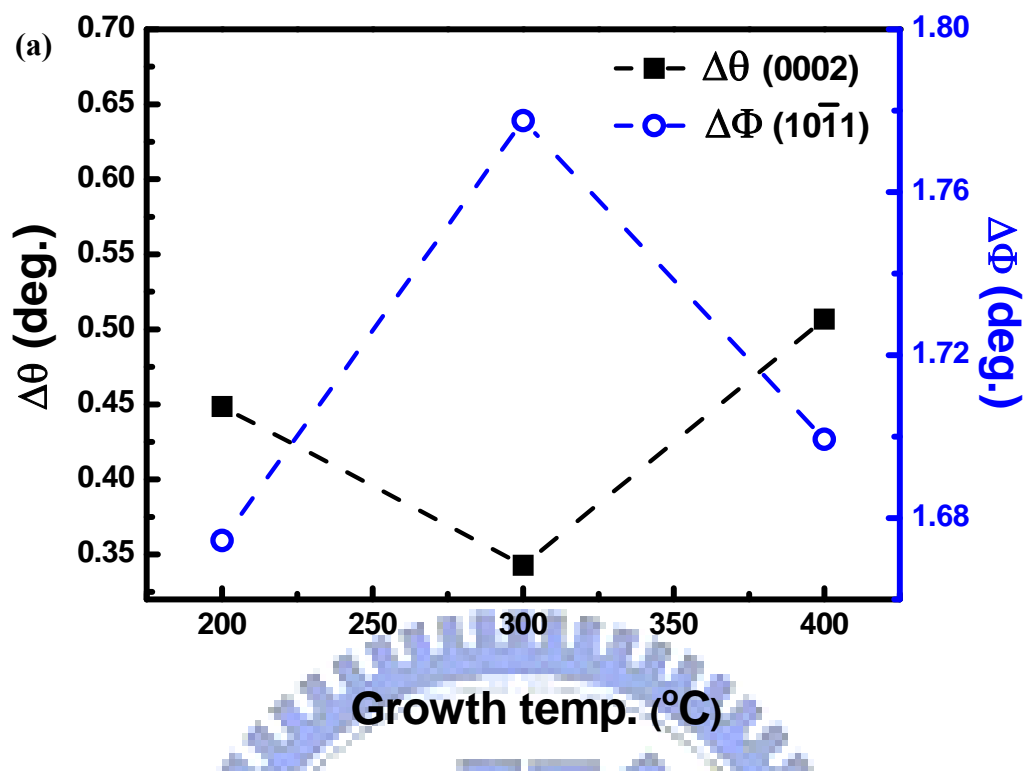


Fig. 4-3(a) Correlation between growth temperature and ZnO $\Delta\theta(0002)$ / $\Delta\Phi$

($10\bar{1}0$) distribution for the first batch of substrate

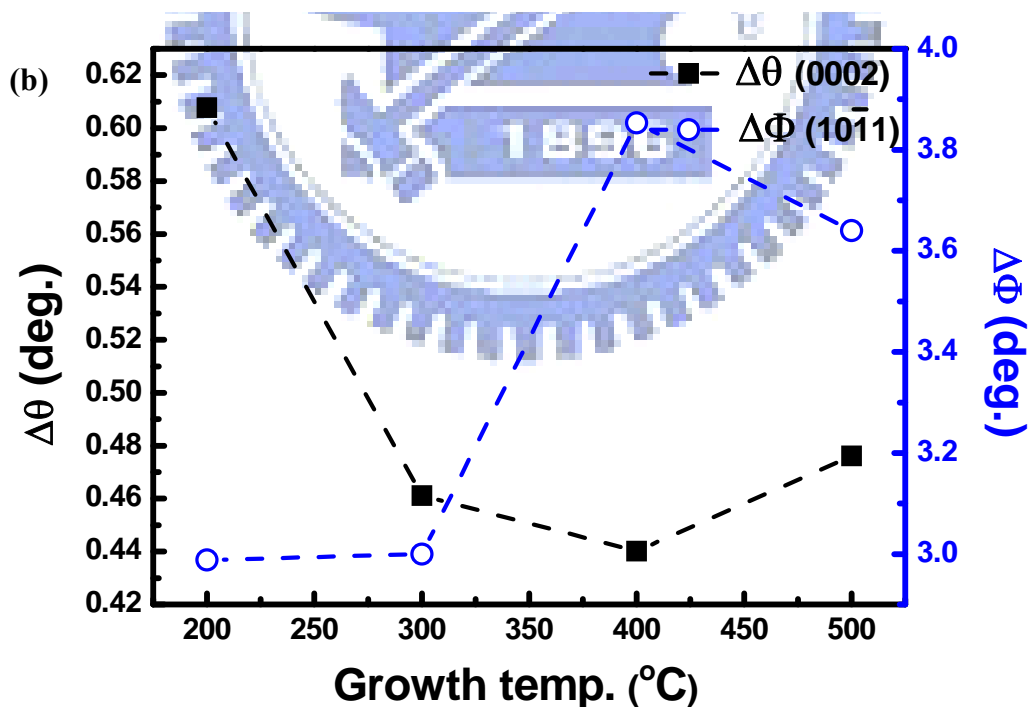


Fig. 4-3(b) Correlation between growth temperature and ZnO $\Delta\theta(0002)$ / $\Delta\Phi$

($10\bar{1}0$) distribution for the second batch of substrate

4-1-2 Analysis of threading dislocation density by XRD

The major defect structure in the ZnO film is TDs. In our case, the majority of TDs have their lines lying along the [0001] growth direction that is the same as the ZnO film grown on commonly used c-sapphire [34]. For a (0001)-oriented thin film with wurtzite structure, the TDs are classified into three different types according to the direction of the corresponding Burgers vector (\mathbf{b}) relative to the [0001] line direction. They are edge, screw and mixed TDs characterized with $\mathbf{b}_E = 1/3 \cdot \langle 11\bar{2}0 \rangle$, $\mathbf{b}_C = \langle 0001 \rangle$ and $\mathbf{b}_M = 1/3 \cdot \langle 11\bar{2}3 \rangle$, respectively, where \mathbf{b}_M is the mix of \mathbf{b}_E and \mathbf{b}_C . In order to address the defect structures of wurtzite ZnO by XRD, rocking curves of the $(h0\bar{h}0)$ and $(000l)$ reflections were measured. Note that the broadening of $(h0\bar{h}0)$ and $(000l)$ rocking curves are associated with the lattice misalignment along the in-plane and growth directions, respectively. In other words, pure edge TDs twist the surrounding ZnO lattice about [0001], leading to the formation of vertical grain boundaries [37, 38, 39] and the $(h0\bar{h}0)$ crystalline planes are distorted. On the other hand, pure screw TDs tilt the ZnO lattice and generate a pure shear strain field [40], causing the $(000l)$ planes being deformed. Thus, we measured the $(h0\bar{h}0)$ and $(000l)$ reflections to investigate the influence of edge and screw TDs, respectively. The FWHMs of the θ -rocking curves of $(h0\bar{h}0) / (000l)$ Bragg peaks reflect the lattice twist/tilt and the line width of their radial scans are related to the lateral/vertical inhomogeneous strain field

and domain size.

To obtain a quantitative results, we employed the Williamson-Hall (WH) plot (Δq vs. q , where $q = 4\pi\sin(2\theta/2)/\lambda$ denoting the scattering vector and Δq is the line width in q along the radial direction) to separate the reflection peak broadening due to finite structural coherent length from strain-induced broadening. According to Eq. 2-6, the inverse of the ordinate intercept yields the coherence length which corresponds to the effective domain size and the slope yields the root-mean-square (rms) inhomogeneous strain. Figures 4-4 (a) and (b) are the typical WH plots of radial scans along the ZnO ($h0\bar{h}0$) and (000 l), respectively. For ZnO film grown at 300°C, the coherence length along surface normal is ~293.6 nm, indicating its structure maintains coherent almost over the entire film thickness. The in-plane domain size is 117 nm. The average lateral strain is $\sim 3.83 \times 10^{-3}$ about three times that along the surface normal ($\sim 1.3 \times 10^{-3}$), indicating that the dominant cause of ZnO lattice distortion comes mainly from edge dislocation. Figures 4.5 (a) and (b) are plots of Δq_t vs. q (where $\Delta q_t = q \cdot \Delta\theta$ denotes the spread of θ in the transverse direction) for θ -rocking scans across the ($h0\bar{h}0$) and (000 l), the slopes yield the spread of twist and tilt angles, respectively. The twist angle (α_ϕ) and tilt angle (α_Ω) of ZnO fall within the ranges of $1.38^\circ \sim 3.8^\circ$ and $0.28^\circ \sim 0.53^\circ$, respectively. Note that for samples grown under different temperatures, the ZnO films exhibit the opposite trend of variation for tilt and twist angles, which are similar to the

trend of θ -rocking curve linewidths of ZnO(0002) and (10 $\bar{1}$ 0) reflections because $\Delta\theta_{(0002)}$ and $\Delta\phi_{(10\bar{1}1)}$ bear the same physical meaning as the tilt and twist angles. The

TD density can be estimated from the corresponding Burgers vectors and tilt or twist angles. The density of screw type dislocations, N_s , is obtained using the equation:

$$N_s = \frac{\alpha_\Omega^2}{4.35b_C^2},$$

where α_Ω is the tilt angle and b_C is the magnitude of the corresponding

Burgers vector \mathbf{b}_C , which is [0001] with $b_C = 0.519$ nm in our case [41]. The edge

type TD density, N_E , can be calculated by adapting $N_E = \frac{\alpha_\phi}{2.1|b_E|L}$, where α_ϕ , b_E and L

are twist angle, the length of corresponding Burgers vector ($b_E = 0.325$ nm) and

correlation length along the in-plane direction, respectively [39]. This formula is

based on the model of dislocation piling up in small angle boundaries and forming

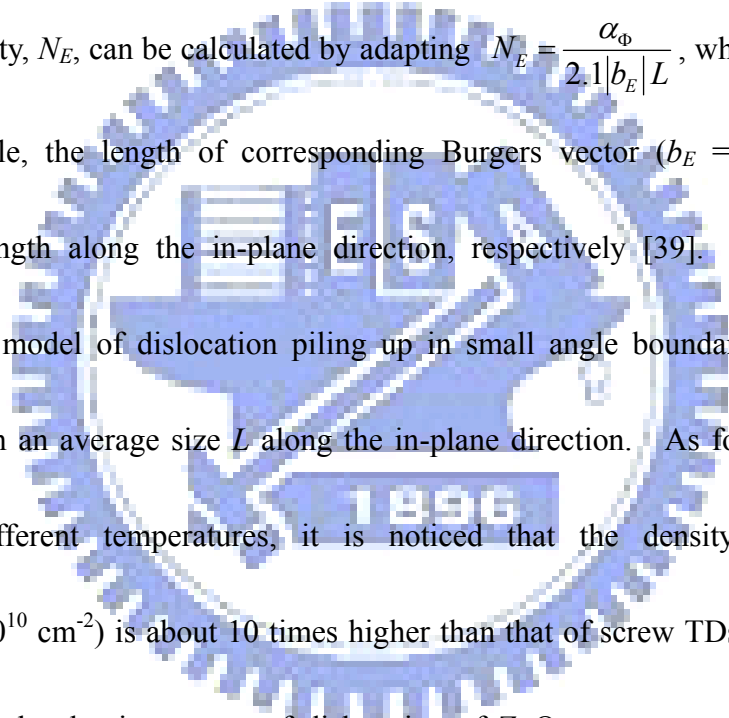
subgrains with an average size L along the in-plane direction. As for our ZnO films

grown at different temperatures, it is noticed that the density of edge TDs

($1.39\sim 9.97\times 10^{10}$ cm $^{-2}$) is about 10 times higher than that of screw TDs ($2.14\sim 5.75\times 10^9$

cm $^{-2}$). Thus, the dominant type of dislocation of ZnO grown on γ -Al $_2$ O $_3$ /Si(111) is

edge TDs. It is the same as the case of ZnO grown on c-sapphire [36].



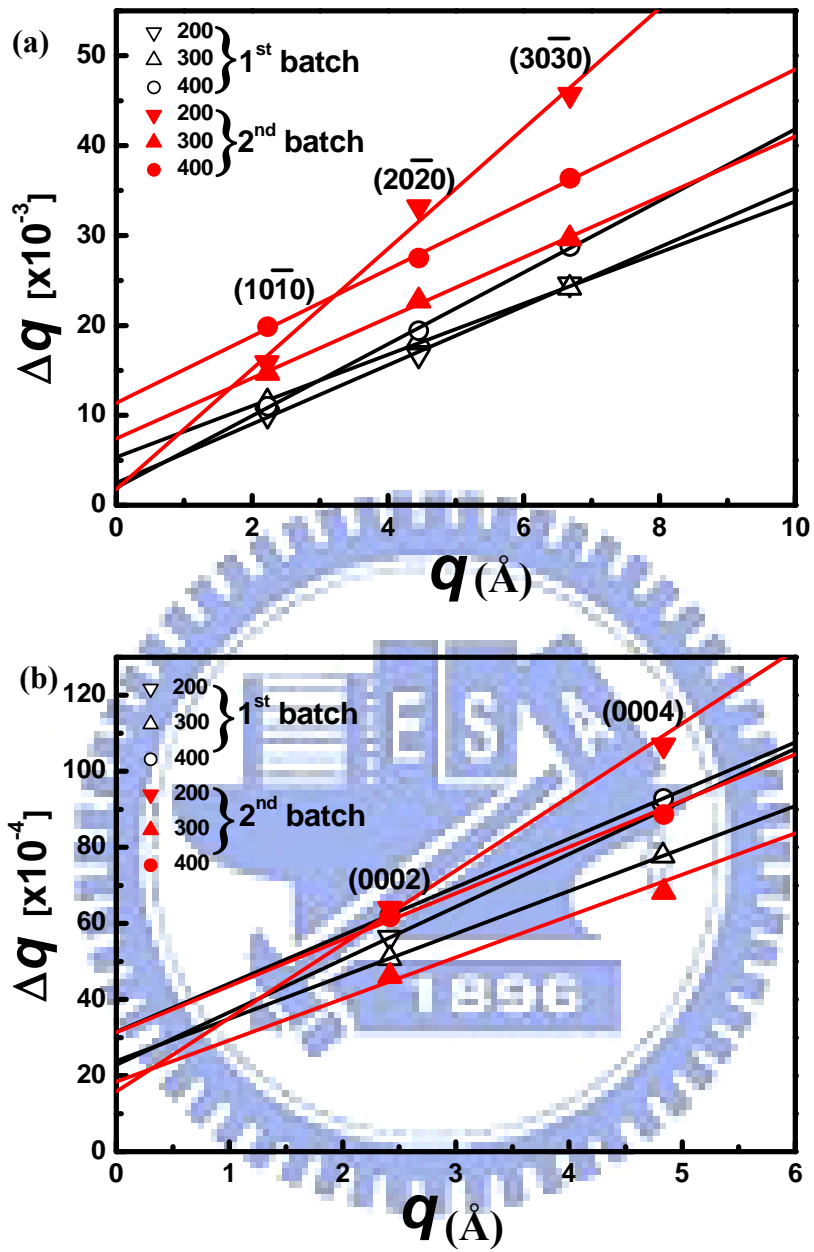


Fig. 4-4 Williamson-Hall plots of ZnO layers grown at various temperatures.

The symmetric radial scans were measured for (a) $(h0\bar{h}0)$ surface peaks and

(b) $(000l)$ normal reflections. Lines are linear fits of the data.

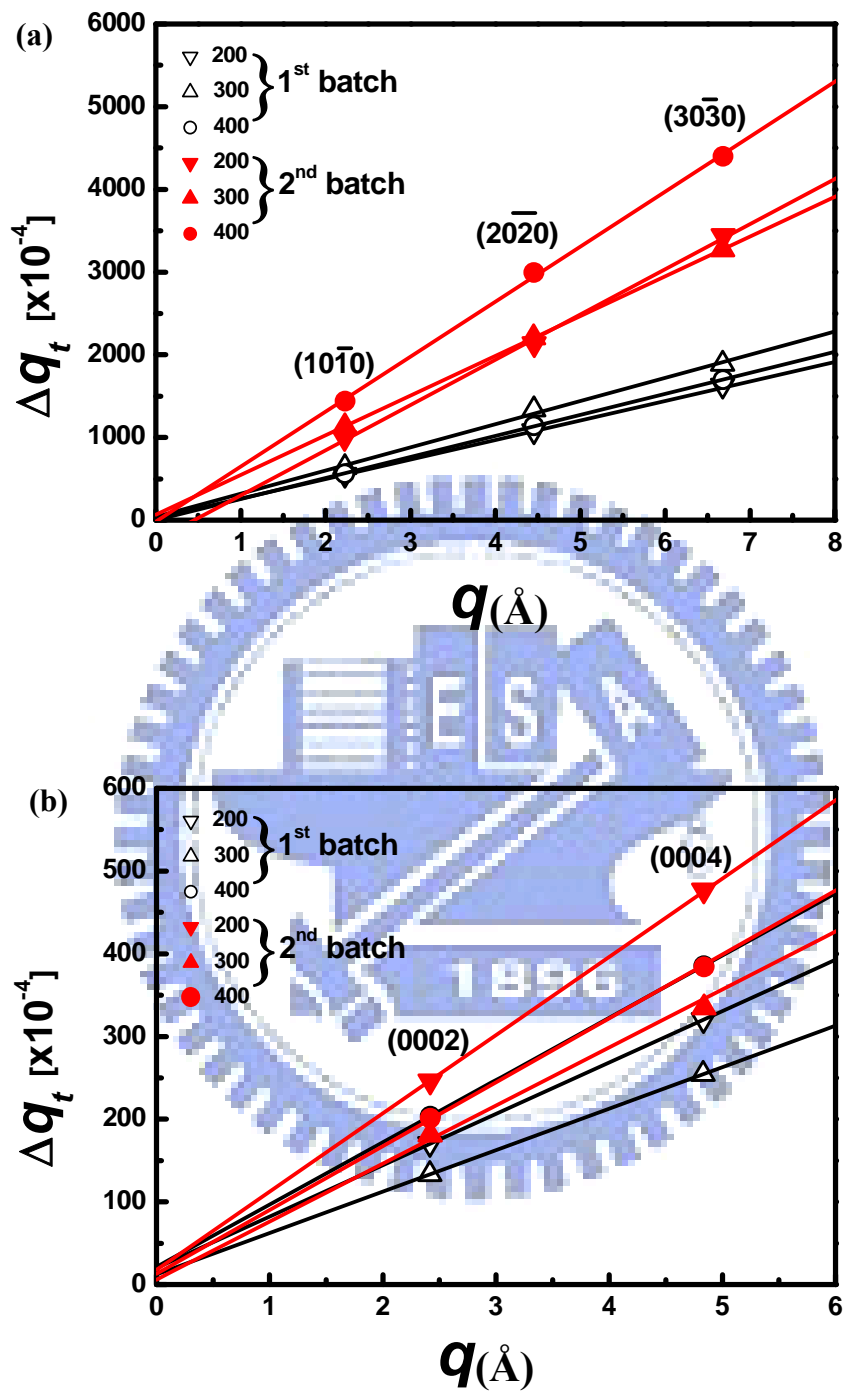


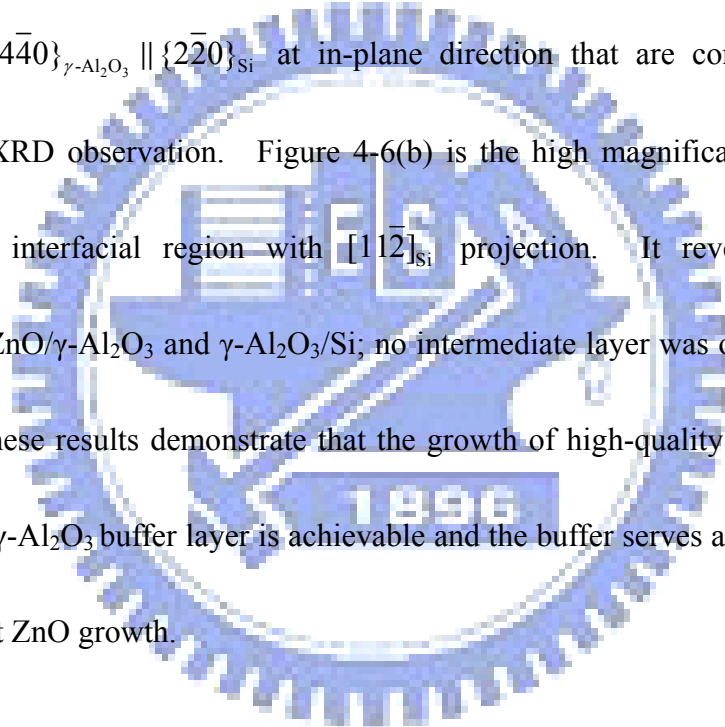
Fig. 4-5 A Δq_t vs. q plot, an analogy to the WH plot for transverse scans, across

(a) surface peaks and (b) normal reflection

4-2 Structural characterization by TEM

4-2-1 cross sectional TEM

Illustrated in Fig. 4-6 (a) is a selected area electron diffraction (SAED) pattern along $[1\bar{1}2]_{\text{Si}}$ direction. The diffraction peaks from Si substrate, $\gamma\text{-Al}_2\text{O}_3$ buffer and ZnO epi-layer can be well identified and confirmed. The crystalline orientation relationship is $(0002)_{\text{ZnO}} \parallel (222)_{\gamma\text{-Al}_2\text{O}_3} \parallel (111)_{\text{Si}}$ at surface normal direction and $\{1\bar{1}20\}_{\text{ZnO}} \parallel \{4\bar{4}0\}_{\gamma\text{-Al}_2\text{O}_3} \parallel \{2\bar{2}0\}_{\text{Si}}$ at in-plane direction that are consistent with the results from XRD observation. Figure 4-6(b) is the high magnification TEM image taken at the interfacial region with $[1\bar{1}2]_{\text{Si}}$ projection. It reveals unequivocal interfaces of ZnO/ $\gamma\text{-Al}_2\text{O}_3$ and $\gamma\text{-Al}_2\text{O}_3/\text{Si}$; no intermediate layer was observed in either interface. These results demonstrate that the growth of high-quality epi-ZnO film on Si by using a $\gamma\text{-Al}_2\text{O}_3$ buffer layer is achievable and the buffer serves as a good template for subsequent ZnO growth.



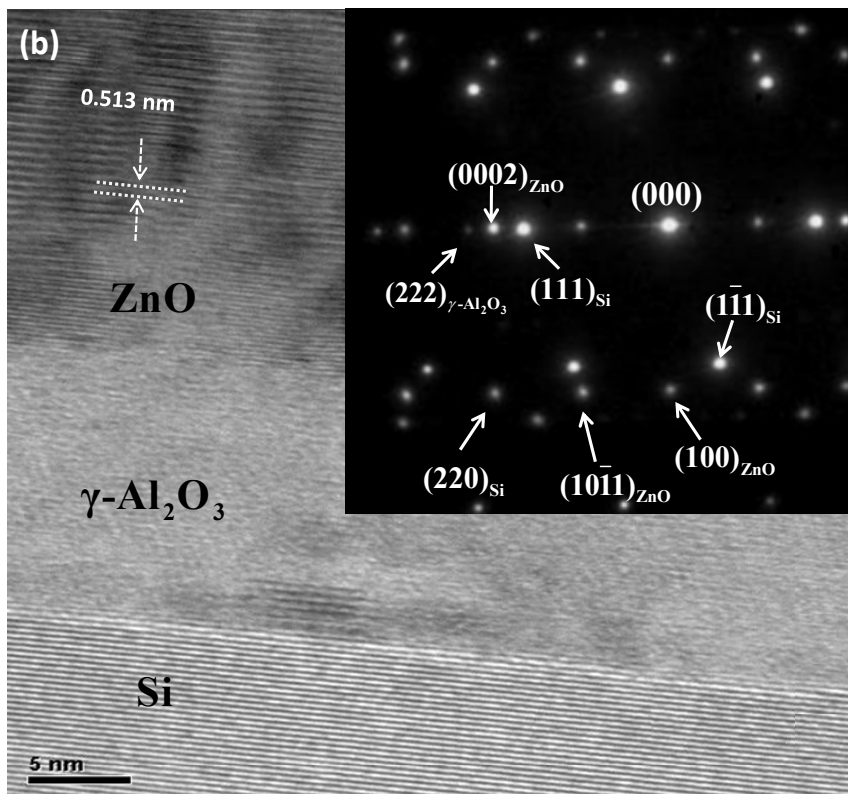
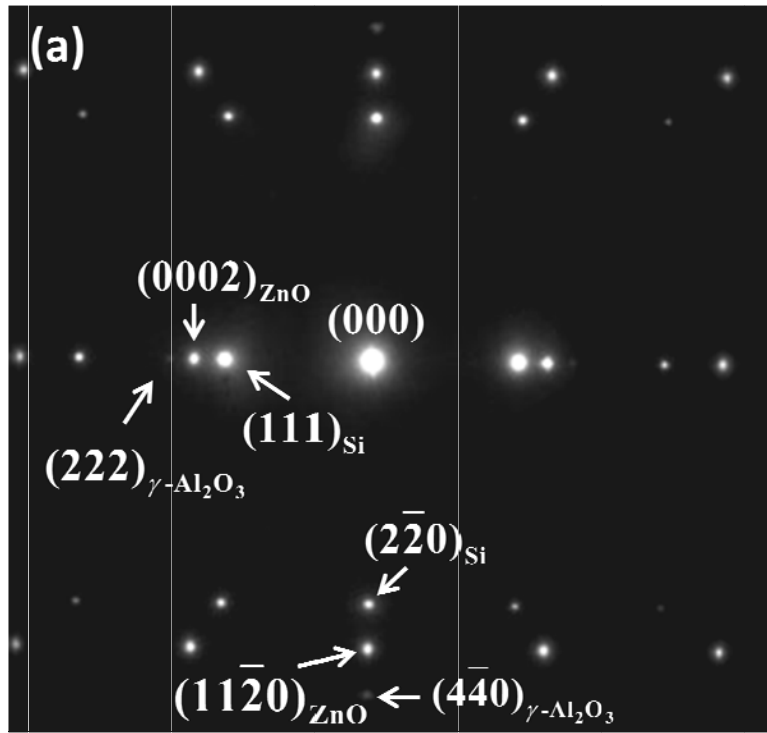
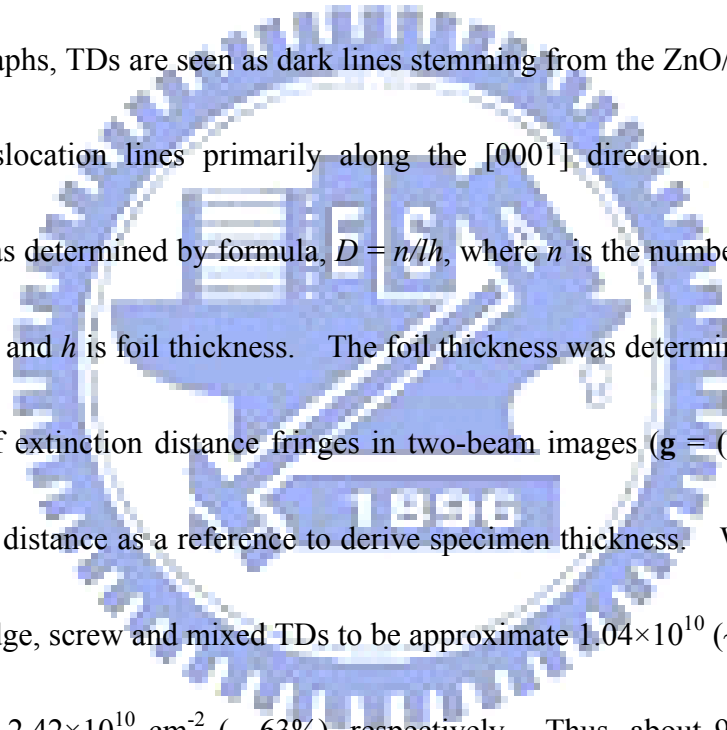


Fig. 4-6 Selected area electron diffraction pattern along $[11\bar{2}]_{Si}$ projection (a) and cross-sectional HR-TEM micrograph taken near the interfacial region with $[10\bar{1}]_{Si}$ projection (b). The inset is the corresponding SAED along $[10\bar{1}]_{Si}$ direction.

4-2-2 Analysis of threading dislocation density

The types of dislocations in ZnO films were further characterized by cross-sectional TEM under a two-beam contrast condition. The diffraction contrast of dislocations in TEM images arises from the bending of lattice planes caused by the dislocation induced strain field. For pure screw dislocations, planes with their normals perpendicular to the Burgers vector \mathbf{b}_C are undistorted. Therefore, all electron beams that are diffracted by planes containing \mathbf{b}_C show no image contrast. With \mathbf{g} being the operating diffraction vector, and \mathbf{b}_C the Burgers vector of the dislocation, the invisibility criterion for pure screw TDs is $\mathbf{g} \cdot \mathbf{b}_C = 0$. For pure edge dislocations, only lattice planes perpendicular to the dislocation line direction will be undistorted and edge dislocations will be invisible in images that are formed using electron beams diffracted from these planes. A pure edge dislocation gives rise to two displacement components of lattice. One is parallel to the Burgers vector \mathbf{b}_E , and the other perpendicular to the slip plane, those normal can be expressed by $\mathbf{b}_E \times \mathbf{u}$ with \mathbf{u} denoting the unit vector along the positive direction of the dislocation line. Therefore, to ensure complete invisibility for an edge dislocation, in addition to $\mathbf{g} \cdot \mathbf{b}_E = 0$, the condition $\mathbf{g} \cdot (\mathbf{b}_E \times \mathbf{u}) = 0$ has to be satisfied, too [27]. Based on these invisibility criteria, we can distinguish the types of the TDs by analyzing images taken with different operating diffraction vector \mathbf{g} . Figures 4-7(a)-(c) show the images of the ZnO film grown at 300°C taken with the diffraction

vector \mathbf{g} equal to ZnO(0002), $(11\bar{2}0)$, and $(11\bar{2}2)$, respectively. According to the invisibility criteria, $\mathbf{g} \cdot \mathbf{b} = 0$, screw type dislocations with $\mathbf{b}_C = \langle 0001 \rangle$ are invisible with $\mathbf{g} = (11\bar{2}0)$ but visible under $\mathbf{g} = (0002)$ and $(11\bar{2}2)$. In contrast, edge type dislocations with $\mathbf{b}_E = 1/3 \cdot \langle 11\bar{2}0 \rangle$ and $(\mathbf{b}_E \times \mathbf{u}) // \langle \bar{1}100 \rangle$ should be invisible under $\mathbf{g} = (0002)$ but visible under $\mathbf{g} = (11\bar{2}0)$ and $(11\bar{2}2)$. As to the TDs of mixed type character with $\mathbf{b}_M = 1/3 \cdot \langle 11\bar{2}3 \rangle$, they are visible under all three \mathbf{g} vectors. In all three micrographs, TDs are seen as dark lines stemming from the ZnO/ γ -Al₂O₃ interface with their dislocation lines primarily along the [0001] direction. The dislocation density, D , was determined by formula, $D = n/lh$, where n is the number of dislocations, l is foil length and h is foil thickness. The foil thickness was determined by measuring the number of extinction distance fringes in two-beam images ($\mathbf{g} = (0002)$) and using the extinction distance as a reference to derive specimen thickness. We calculated the densities of edge, screw and mixed TDs to be approximate 1.04×10^{10} (~ 27%), 3.46×10^9 (~ 10%), and $2.42 \times 10^{10} \text{ cm}^{-2}$ (~ 63%), respectively. Thus, about 90% of total TDs contain the edge component consistent with the result calculated from XRD data that edge is the dominant type TDs.



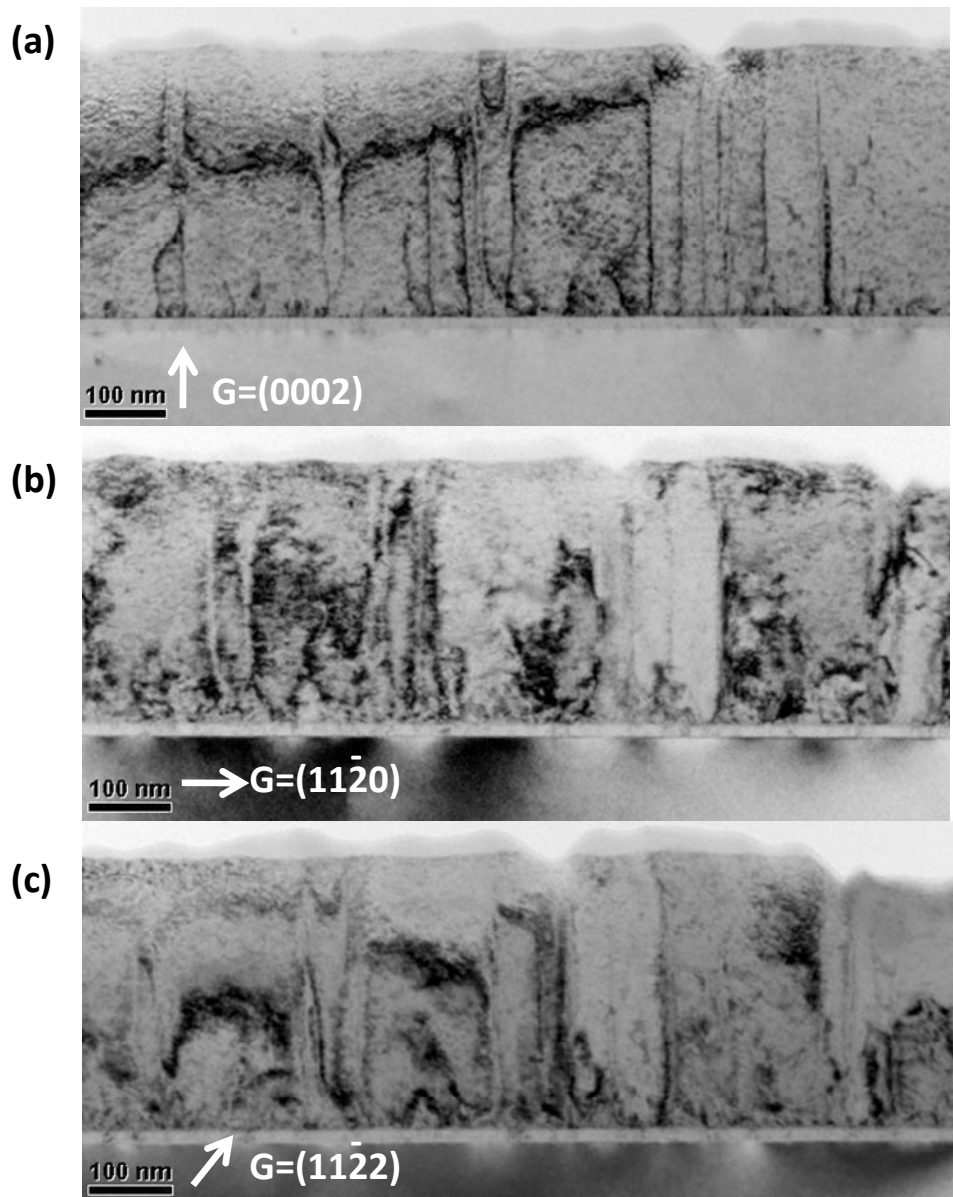


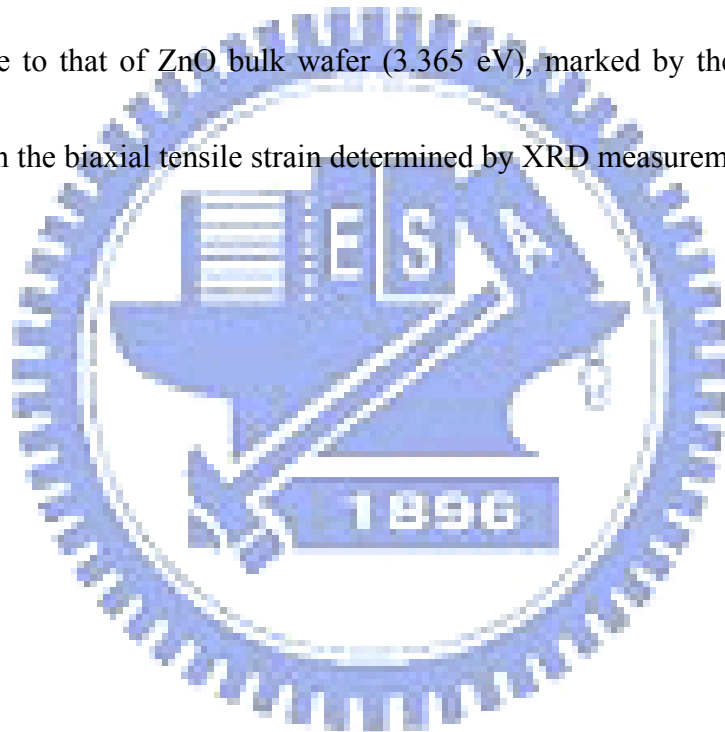
Fig. 4-7 Two-beam bright field cross sectional micrograph of a ZnO thin film taken with (a) $g = (0002)$, (b) $g = (11\bar{2}0)$ and (c) $g = (11\bar{2}2)$.

4-3 Optical characterization by PL

4-3-1 Photoluminescence spectra of as-grown films

We carried out low temperature (LT) PL at 15K to characterize the optical properties of the ZnO films. The PL spectra of ZnO films are shown in Fig. 4-8. Regardless of the growth temperatures, the main features on PL spectra are common for all samples. The spectra can be divided into two parts: sharp near band-edge emission (NBE) and broad deep level emission (DLE), which are centered at ~ 3.365 and ~ 2.196 eV, respectively. The dominant peak at NBE region is attributed to the recombination of excitons bound to neutral donor (D^0X) [42] and the broad DLE results from point defects such as O vacancies and Zn interstitials [43]. The assignments of NBE peaks are also shown in Fig. 4-9, which is the PL spectrum of the ZnO grown at 300°C. The peak at 3.375 eV was designated as the free A-exciton (FX_A) line; the binding energy of the corresponding A-exciton was obtained to be 58.875 meV by fitting the temperature dependent PL data using the Arrhenius expression, as shown in Fig. 4-10. The dominant peak at ~ 3.364 eV in the NBE region was assigned to the recombination of excitons bound to neutral donor (D^0X) [44] and its FWHM is 9.4 meV. The D^0X emission accompanied with single phonon (D^0X-1LO) and dual phonon (D^0X-2LO) replica appear at 3.288 and 3.215 eV. The peak at ~ 3.23 eV is attributed to the donor-acceptor pair (DAP) transition. Another strong line at 3.328 eV originates from

the transition involving radiative recombination of an exciton bound to a neutral donor (D^0X) and leaving the donor in the excited state. This process is also known as the two-electron satellite (TES). We made such an assignment based on the ratio of donor binding energy to exciton binding energy ~ 0.35 , as reported by Teke et al [42]. Similarly to the E2-high mode in the Raman spectra of ZnO thin films [43], the position of the D^0X is sensitive to the strain state of the films. The observed red shift of D^0X energy relative to that of ZnO bulk wafer (3.365 eV), marked by the dashed lines, is consistent with the biaxial tensile strain determined by XRD measurements.



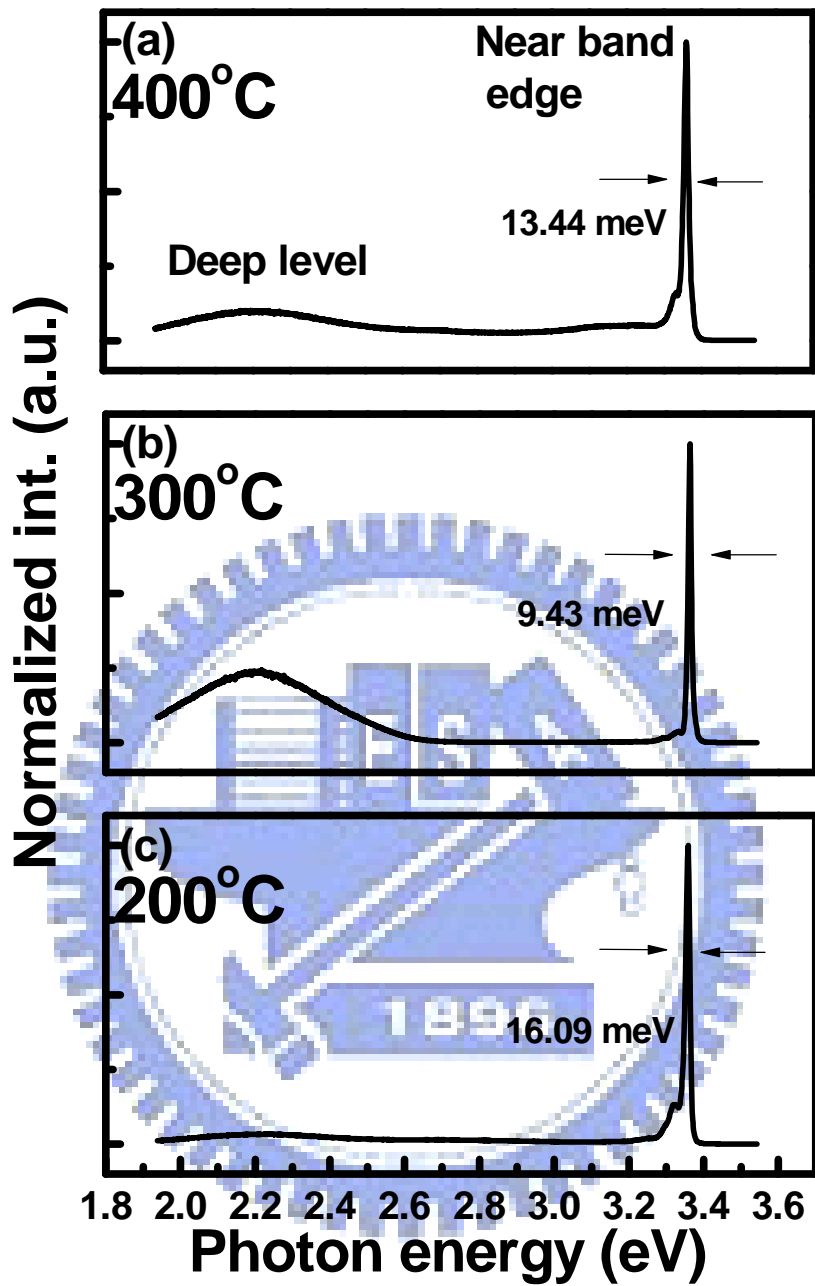


Fig. 4-8 Typically PL spectra measured at 15K for ZnO epi-layers deposited on γ -Al₂O₃/Si (111) at (a) 200°C, (b) 300°C and (c) 400°C, respectively. The spectra can be divided into two major parts: NBE and DLE. The FWHMs of NBE are marked near the peaks.

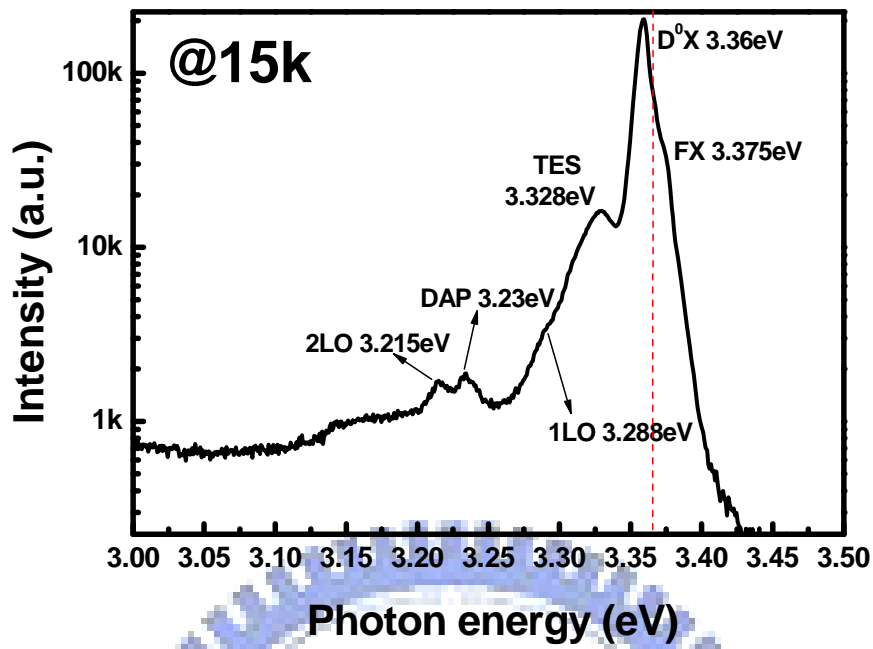


Fig. 4-9 The extended spectra of NBE emission of ZnO grown at 300°C. The dashed line marks the D°X peak position of bulk ZnO.

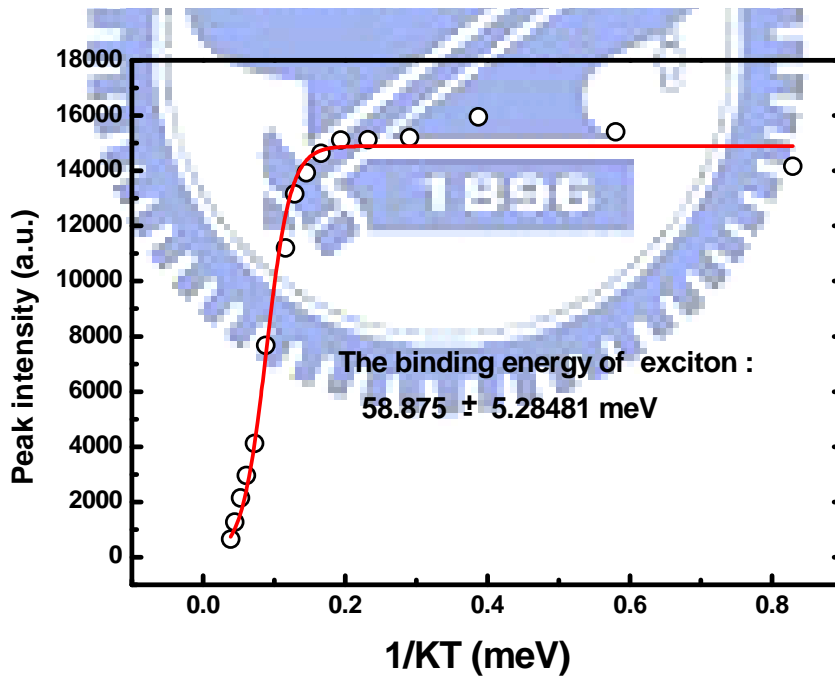


Fig. 4-10 Dependence of FX_A PL peak intensity on sample temperature for the ZnO film grown at 300°C.

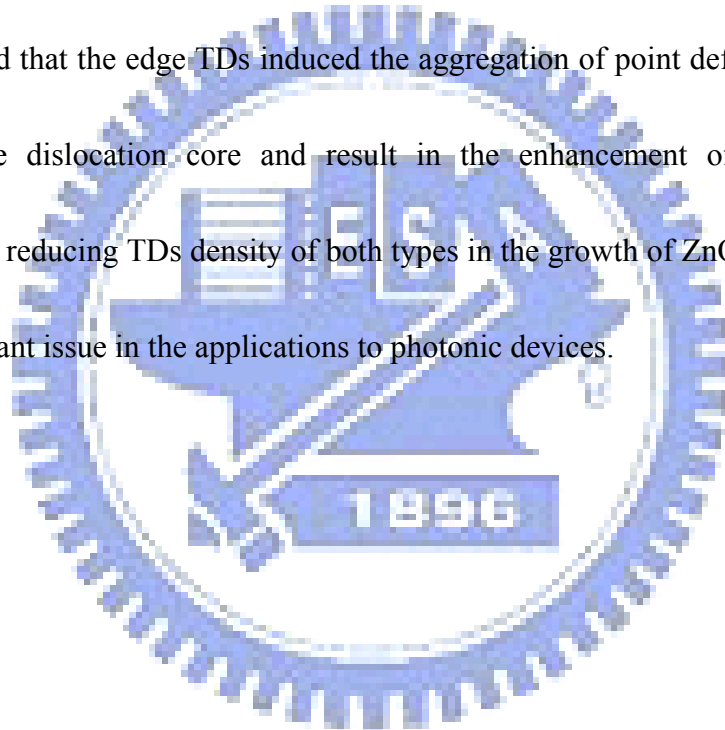
4-4 Correlation between structural and optical properties of ZnO films

The ZnO films with narrower FWHM of NBE and lower ratio of DLE to NBE intensity (I_{DLE}/I_{NBE}) are considered to have better optical properties. For the ZnO films grown at different temperatures and on different batches of γ -Al₂O₃/Si substrates, we found that the optical performance of films grown at 300°C always exhibits the best characteristics in NBE region but the worst in DLE region among the samples grown on the same substrate. In other words, FWHM of NBE and (I_{DLE}/I_{NBE}) ratio exhibited an opposite trend of variation vs. growth condition. From the previous XRD results, we also observed the opposite trend of $\Delta\theta_{(0002)}$ and $\Delta\phi_{(10\bar{1}1)}$ for our specimen. The (I_{DLE}/I_{NBE}) ratio versus $\Delta\phi_{(10\bar{1}1)}$, the FWHM of the azimuthal scan across ZnO off-normal $(10\bar{1}0)$ reflection, and the FWHM of NBE versus $\Delta\theta_{(0002)}$, the FWHM of the rocking curve of the (0002) specular reflection, are illustrated in Figs. 4-11(a) and (b), respectively. Here, $\Delta\theta_{(0002)}/\Delta\phi_{(10\bar{1}1)}$ bears the same physical meaning as the tilt/twist angle. Besides, tilt angle is coupled with screw type TDs while twist angle is coupled with edge type TDs. It suggests that we can individually observe the influence of different types of TDs on the optical property of ZnO film grown on γ -Al₂O₃/Si(111). Figure 4-12(a) shows the correlation between (I_{DLE}/I_{NBE}) ratio and edge dislocation density. It elucidates that the ZnO with larger (I_{DLE}/I_{NBE}) ratio

possesses the higher edge dislocation density. Figure 4-12(b) displays the FWHM of NBE as a function of screw dislocation density. Similarly, it exhibits a positive correlation between them. In contrast, both (I_{DLE}/I_{NBE}) ratio vs. screw dislocation density and NBE line width vs. edge dislocation density plots do not show any clear correlation, as shown in Figs. 4-11(c) and (d). Thus, it is evident that the NBE is dominantly affected by screw type TDs and DLE is mainly influenced by edge type TDs.

It is speculated that the edge TDs induced the aggregation of point defects due to stress field near the dislocation core and result in the enhancement of DLE intensity.

Consequently, reducing TDs density of both types in the growth of ZnO epitaxial film is still an important issue in the applications to photonic devices.



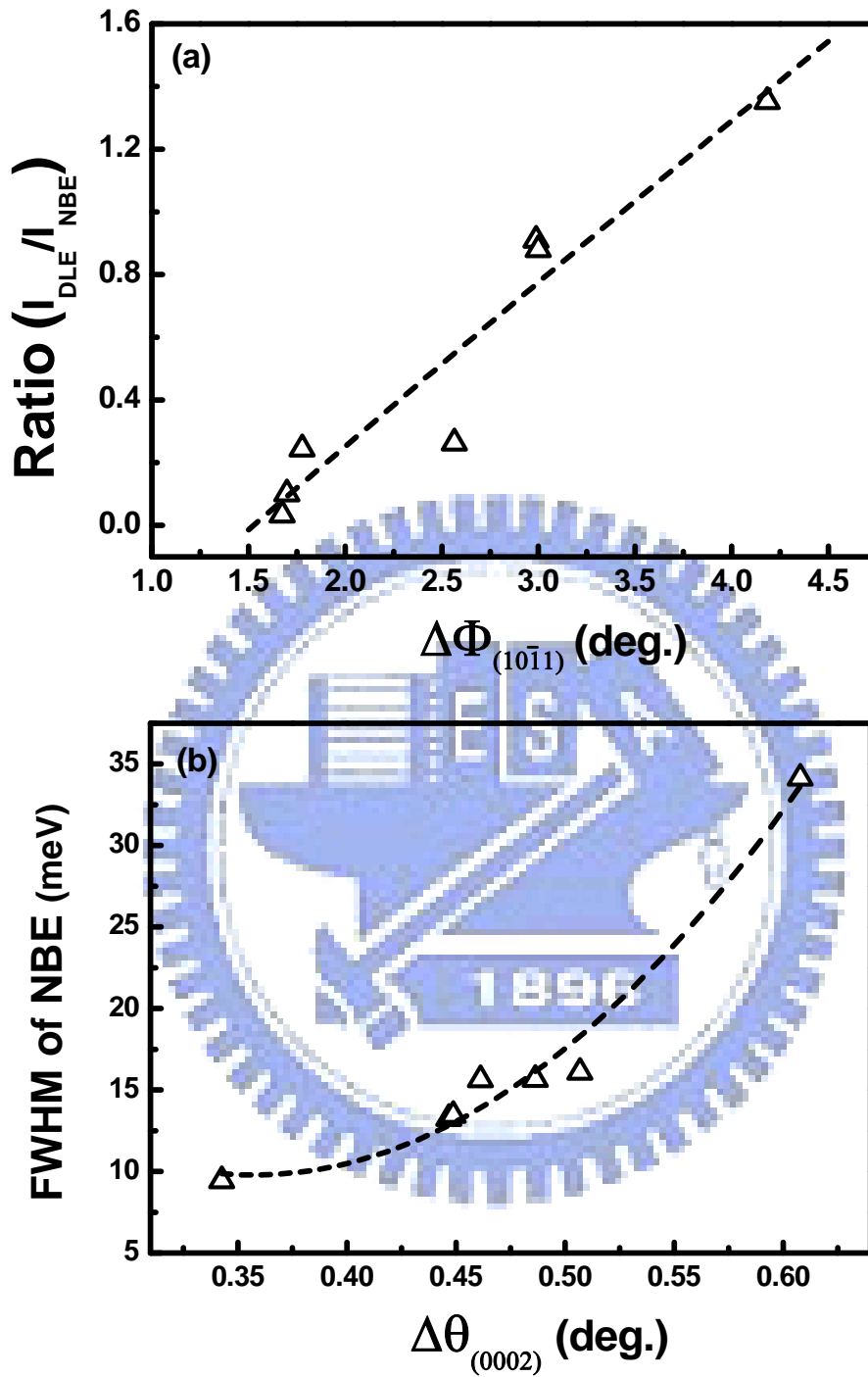


Fig. 4-11 The dependence of (I_{DLE}/I_{NBE}) ratio on $\Delta\phi_{(10\bar{1}1)}$ (a) and the dependence of NBE width $\Delta\theta_{(0002)}$ (b). The dashed curves were plotted to guide the eyes.

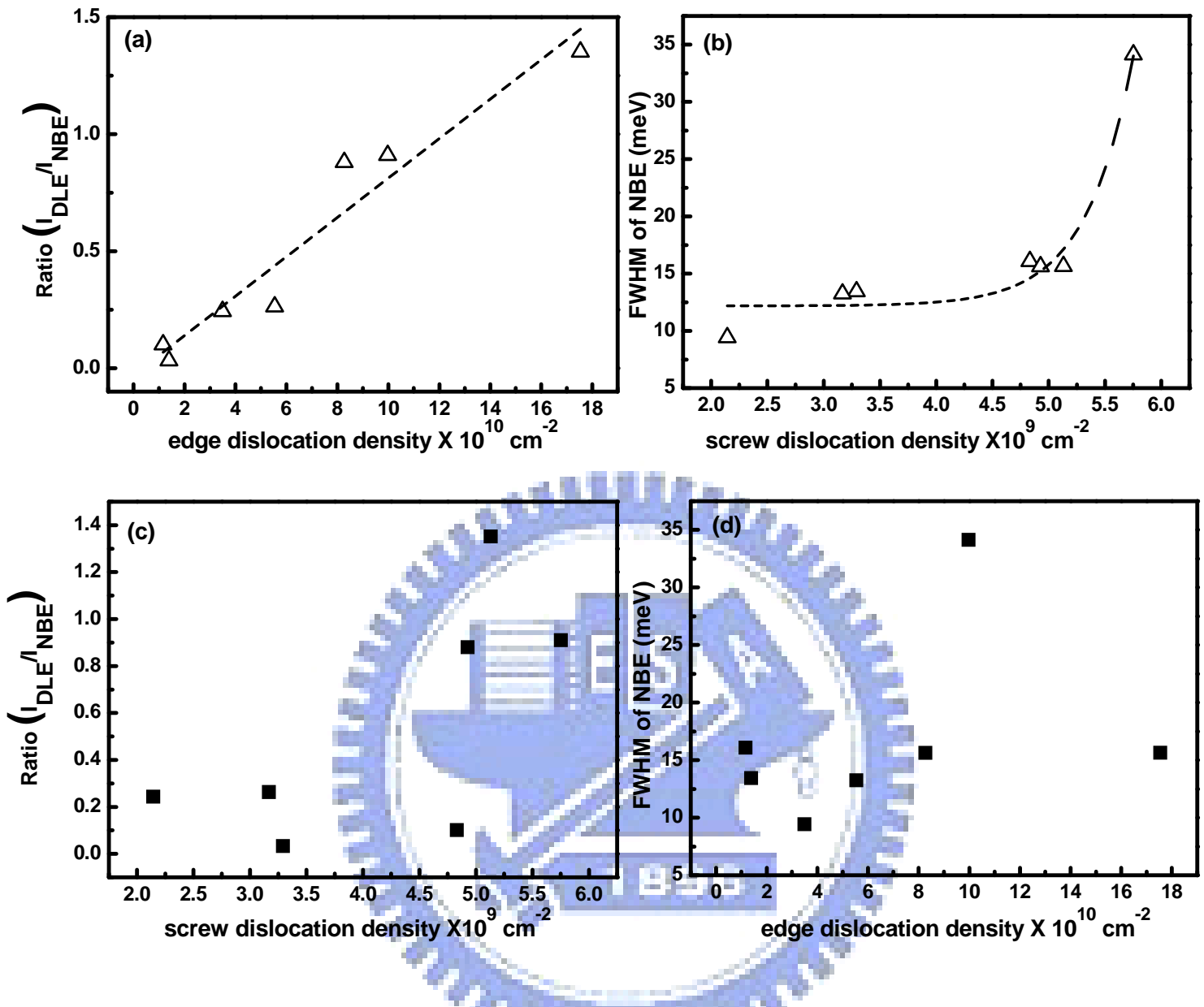


Fig. 4-12 PL (I_{DLE}/I_{NBE}) intensity ratio vs. edge dislocation density plot (a); NBE FWHMs vs. screw dislocation density (b), the dashed curves were fitted to guide the eyes. (c) and (d) are the plots of exchanging abscissa of (a) and (b). There is no obvious correlation after exchanging the abscissas.

Chapter 5 Conclusions and Perspective

5-1 Conclusions

High-quality ZnO epitaxial films have been successfully grown by pulse laser deposition on Si(111) substrates with a thin oxide γ -Al₂O₃ buffer layer. There are two (111)-oriented γ -Al₂O₃ domains rotated 60 degrees from each other relative to the surface normal. The in-plane epitaxial relationship between the wurtzite ZnO, cubic γ -Al₂O₃ and cubic Si follows $\{10\bar{1}0\}_{\text{ZnO}} \parallel \{22\bar{4}\}_{\gamma\text{-Al}_2\text{O}_3} \parallel \{22\bar{4}\}_{\text{Si}}$ and $\{10\bar{1}0\}_{\text{ZnO}} \parallel \{4\bar{2}\bar{2}\}_{\gamma\text{-Al}_2\text{O}_3} \parallel \{22\bar{4}\}_{\text{Si}}$ coexist. XRD and TEM measurements reveal that the main defect structures in ZnO films are edge TDs. According to the XRD, TEM and LT-PL results, we established the correlation between influence of different types of TDs and optical properties of the ZnO epi-films. Our results demonstrated that the ratio ($I_{\text{DLE}}/I_{\text{NBE}}$) is mainly affected by edge TDs and the FWHM of NBE is dominantly influenced by screw TDs. The reduction of the dislocation density is one of the most important factors to improve the ZnO-based optical device.

5-2 Perspective

In our research, we have derived the relationship between the photoluminescence and structural properties of ZnO films. It is always speculated that the DLE is coupled with the point defects such as O vacancies and Zn interstitials and aging in air can

improve the optical properties of ZnO layer has been reported [46]. We therefore performed post growth thermal annealing in an oxygen ambient (800 °C in 1 atm O₂ for 100 min.) and the optical performance of all the samples exhibited evident improvement. Take a 270 nm thick sample grown at 300°C as an example, its PL spectra measured before and after thermal annealing are displayed in Fig. 5-1(a) and (b), respectively; significant reduction of the DLE signals and narrower FWHM of NBE were observed after the annealing. We also annealed a similarly prepared sample in N₂ atmosphere; the PL spectrum was much worse than the one before annealing especially a huge broad peak appeared in the DLE region. These observations supported the argument that the oxygen vacancies played the most important role in the native defects in ZnO thin films deposited by PLD [46].

It is known that ZnO epi-layers with larger thickness usually have better structural characteristics and optical properties. We thus grew a series of samples with various thickness to examine if thermal annealing has the same effect on them. Figures 5-2(a), (b) and (c) are PL spectra of samples before annealing with different thickness ~37, 165 and 300 nm, respectively. The corresponding PL spectra of these samples after annealing are (a'), (b') and (c'). We can clearly observe the reduced DLE and better NBE performance after annealing. Figures 5-3(a) and (b) depict the tilt and twist angles, respectively, as a function of ZnO film thickness before and after thermal

annealing. We can clearly tell for films of thickness less than ~ 200 nm their structural properties improve after annealing and the thinner the ZnO layer the better is the structural improvement. On the other hand, for the ZnO film of thickness ~ 300 nm, the structural property even became worse after annealing but the undesirable DLE was reduced in the PL measurement indicating the improvement in the optical performance. The inconsistency in structural and optical variation may be attributed to the different probing depth of XRD and PL as well as the non-uniformity of the annealing effect to the thick films. Figure 5-4(a) is the x-ray reflectivity curve of a ~ 300 nm thick ZnO film prior thermal annealing. Only a periodic feature yielding a thickness of ~ 10 nm, which is consistent with the thickness of the γ -Al₂O₃ buffer layer, can be identified. After annealing, additional oscillations with a smaller periodicity appeared in the reflectivity curve, as illustrated in Fig. 5-4(b), and all the oscillations became more pronounced indicating smoother interfaces. The presence of the finer fringes revealed the appearance of an extra layer of thickness ~ 98 nm near the surface after annealing. This observation suggests that under the employed annealing treatment, the ZnO film was split into two parts and the oxygen atoms can penetrate into the ZnO film as far as ~ 98 nm in depth to form the upper layer. Thus, the upper layer was annealed under an oxygen rich circumstance and most defect structure was eliminated. The defect structure in the lower layer was not improved or even got worse due to the oxygen

deficient annealing environment. Typically, the PL measurement can only probe a region about 100 nm thick but X-ray can easily penetrate into the sample over several hundreds of nanometers. Therefore, for the thinnest film (~37 nm thick), the whole ZnO layer was nicely annealed in an oxygen rich environment and both XRD and PL were sampling this layer with improved structural and optical properties. In contrast, for the thickest film (~300 nm thick), PL signals were predominantly coming from the ~100 nm thick upper layer but XRD data were an average over the upper layer and the twice thick bottom layer which had worse characteristics in structure and optical performance. As to the sample with medium thickness (~165 nm thick), the PL spectrum is similar to that of the other two samples but only mild improvement in structure was observed as a result of an ensemble average between the more perfect upper layer and the worse bottom layer. That adapted thermal treatment only improves film structure over a finite thickness provides a reasonable explanation to the inconsistency trend found in structural and optical properties as a function of film thickness.

According to this phenomenon, we supposed that we could calculate the diffusion velocity of oxygen in ZnO film by implementing time dependent annealing process. Besides, by implementing the (short)-time dependent annealing of ZnO film with defect rich, we could get the rough information about how depth the PL measurement can

detect and reflect a measurable signal of DLE.

In the future, we could also work on the ZnO based LED as we can successfully grow P-type ZnO film on silicon based system.



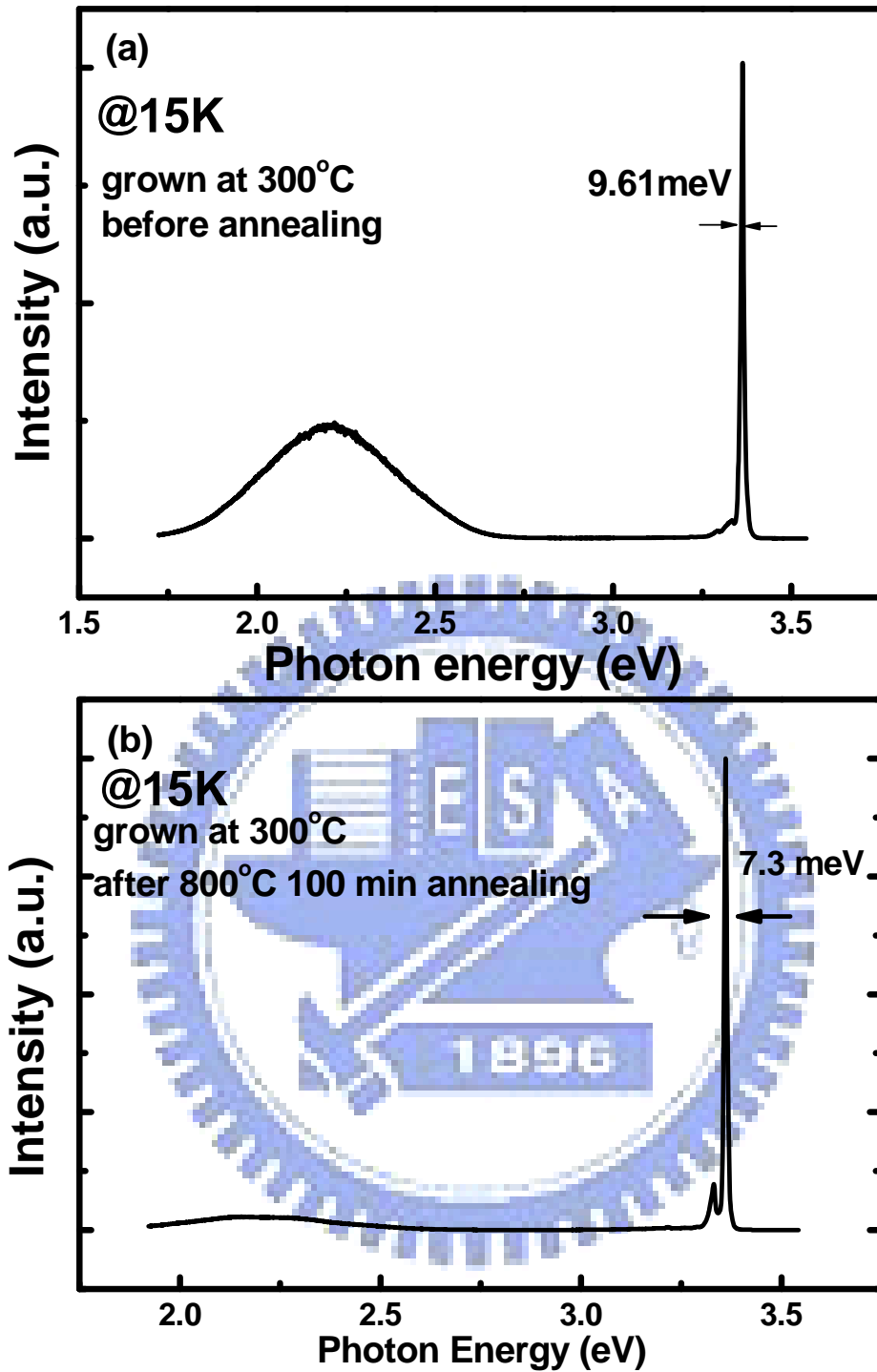


Fig. 5-1 PL spectra measured at 15K of ZnO film grown at 300°C before annealing (a) and after annealing (b). The DLE is obviously reduced and the FWHM of NBE becomes narrower.

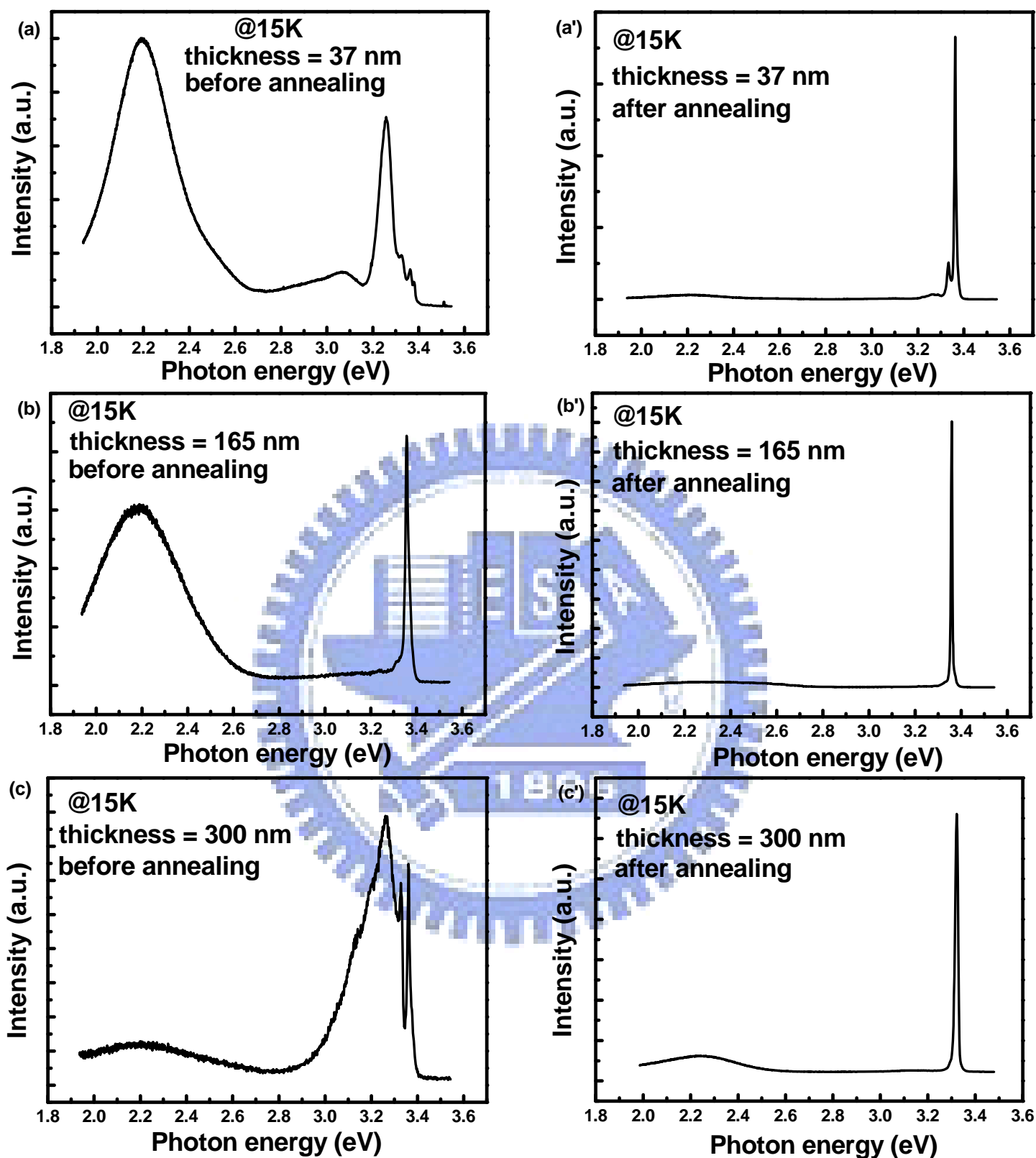


Fig. 5-2 PL spectra measured at 15K of ZnO film grown at 300°C with different thickness before annealing: (a) 37 nm, (b) 165 nm, and (c) 300 nm. The right plots (a'), (b'), and (c') are samples after annealing and are correspond to (a), (b) and (c), respectively.

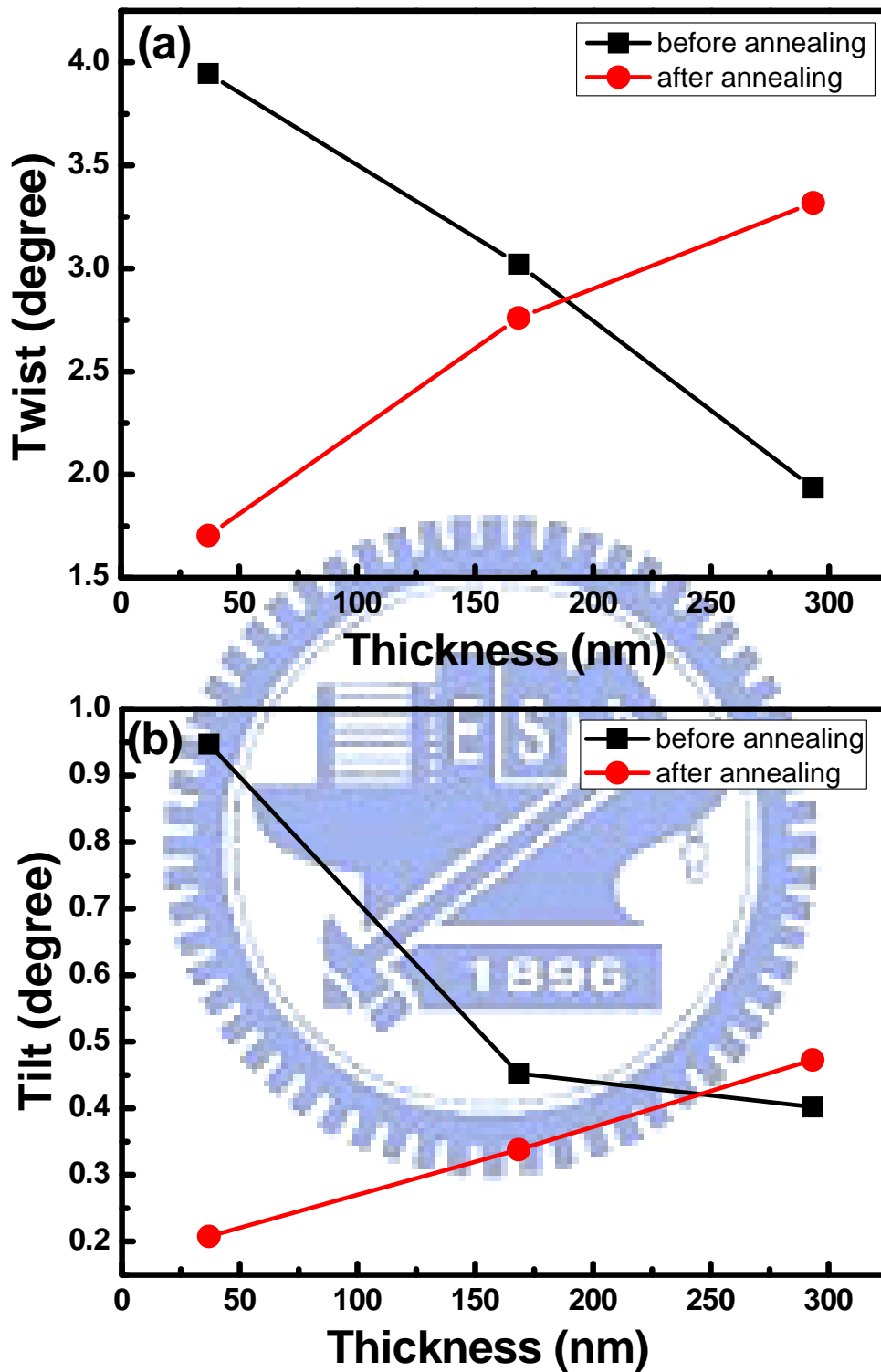


Fig. 5-3 Twist (a) and tilt (b) angles of ZnO films grown with different thickness. The black curves are ZnO films before annealing while the red ones are after annealing.

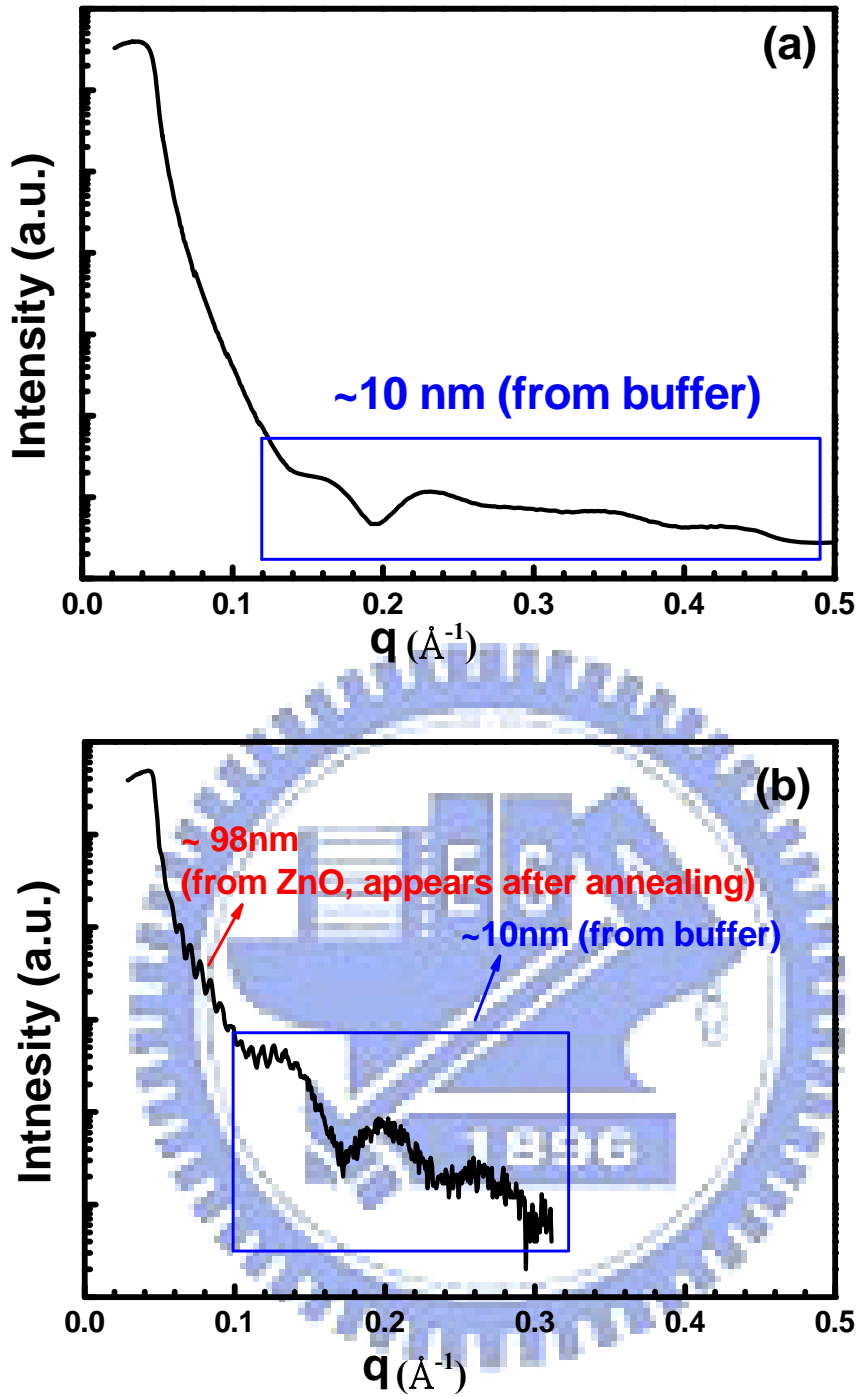


Fig. 5-4 X-ray reflectivity curves of samples (a) before and (b) after annealing. We can clearly observe the presence of extra fringes after annealing in (b). The extra fringes yields a thickness of ~98nm. In both (a) and (b), there always exist fringes, enclosed by rectangle, which corresponds to a layer of thickness ~ 10 nm. This is originated from buffer layer.

References

- [1] Z. K. Tang, G. K. L. Wang, and P. Yu, *Appl. Phys. Lett.* **72**, 3270, 1998.
- [2] Yefan Chen, D. M. Bagnall, Hang-jun Koh, Ki-tae Park, Kenji Hiraga, Ziqiang Zhu, and Takafumi Yao, *J. App Phy.* **84**, 7, 1998.
- [3] D. M. Bagnall, Y. F. Chen, and Z. Zhu, *Appl. Phys. Lett.* **70**, 17, 1997.
- [4] M. Kawasaki, and Y. Segawa, *Phys. Stat. Sol (b)* **202**, 669, 1997.
- [5] Y. Chen, H. Ko, S. Hong, and T. Yao, *Appl. Phys. Lett.* **76**, 559, 2000.
- [6] K. Ogata, T. Kawanishi, K. Maejima, K. Sakurai, Shizuo Fujita and Shigeo Fujita, *Jpn. J. Appl. Phys.* **40**, L657, 2001.
- [7] I. Yamauchi, S. Ueyama and I. Ohnaka, *Mater. Sci. Eng. A* **208**, 108, 1996.
- [8] Y. Z. Yoo, T. Sekiguchi, T. Chikyow, M. Kawasaki, T. Onuma, S. F. Chichibu, J. H. Song, and H. Koinuma, *Appl. Phys. Lett.* **84**, 502, 2004.
- [9] C.C. Lin, S. Y. Chen, S. Y. Cheng, and H. Y. Lee, *Appl. Phys. Lett.* **84**, 5040, 2004.
- [10] H. M. Cheng, H. C. Hsu, S. Yang, C. Y. Wu, Y. C. Lee, L. J. Lin, and W. F. Hsieh, *Nanotechnology* **16**, 2882, 2005.
- [11] M. Fujita, N. Kawamoto, M. Sasajima, and Y. Horikoshi, *J. Vac. Sci. Technol. B* **22**, 1484, 2004.
- [12] X. N. Wang, *Appl. Phys. Lett.* **90**, 151912, 2007.
- [13] R. D. Vispute, *Appl. Phys. Lett.* **73**, 348, 1998.

- [14] A. Nahhas, H. K. Kim, and J. Blachere J, Appl. Phys. Lett. **78**, 1511, 2001.
- [15] Y. Oyama, J. Nishizawa, T. Kimura, and T. Tanno, Phys. Rev. B **74**, 235210, 2006.
- [16] U. Bangert, A. J. Harvey, R. Jones, C. J. Fall, A. Blumenau, R. Briddon, M. Schreck, and F. Hormann, New J. Phys. **6**, 184, 2004.
- [17] H. M. Ng, D. Doppalapudi, T. D. Moustakas, N. G. Weimann, and L. F. Eastman, Appl. Phys. Lett. **73**, 821, 1998.
- [18] J. Y. Shi, L. P. Yu, Y. Z. Wang, G. Y. Zhang, and H. Zhang, Appl. Phys. Lett. **80**, 2293, 2002.
- [19] B. D. Cullity, Element of Xray diffraction, 2nd ed, (Addison Wesley, Cabada, 1978)
- [20] Callister, D. Jr. William, "Fundamentals of Materials Science and Engineering." John Wiley & Sons, Inc. Danvers, MA. (2005)
- [21] B. Heying, X. H. Wu, S. Keller, Y. Li, D. Kapolnek, B. P. Keller, S. P. DenBaars, and J. S. Speck, Appl. Phys. Lett. **68**, 643, 1996.
- [22] F. Vigué, P. Vennéguès, S. Vézian, M. Laügt, and J. P. Faürie, Appl. Phys. Lett. **79**, 194, 2001.
- [23] V. Strikant, J. S. Speck, and D. R. Clarke, J. Appl. Phys. **82**, 4286, 2002.
- [24] G. K. Williamson, and W. H. Hall, Acta Metall. **1**, 22, 1953.
- [25] P. Gay, P. B. Hirsch, and A. Kelly, Acta Metall. **1**, 315, 1953.
- [26] H. J. Hordon, and B. L. Averbach, Acta Met. **9**, 237, 1961.

- [27] B. Fultz, J. Howe, Transmission Electron Microscopy and Diffractometry of Materials, Springer, 2000.
- [28] D. B. Williams, and C. B. Carter, Transmission Electron Microscopy, 1997: Plenum.
- [29] S. Y. Wu, M. Hong, A. R. Kortan, J. Kwo, J. P. Mannaerts, W. C. Lee, and Y. L. Huang (2005). Appl. Phys. Lett. **87**, 091908.
- [30] M. Hong, M. Passlack, J. P. Mannaerts, J. Kwo, S. N. G. Chu, N. Moriya, S. Y. Hou, and V. J. Fratello, J. Vac. Sci. Technol. B **14**, 2297, 1996.
- [31] W. Kollenberg, and J. Margalit, J. Mater. Sci. Lett. **11**, 991, 1992.
- [32] R. T. Tung, and J. L. Batstone, Appl. Phys. Lett. **52**, 1611, 1988.
- [33] Y. Z. Yoo, T. Sekiguchi, T. Chikyow, M. Kawasaki, J. H. Song, and H. Koinuma, Appl. Phys. Lett. **84**, 502, 2004.
- [34] Y. Chen, F. Jiang, L. Wang, C. Zheng, J. Dai, Y. Pu, and W. Fang, J. Cryst. Growth **275**, 486, 2005.
- [35] J. Zhu, B. Lin, X. Sun, R. Yao, C. Shi, and Z. Fu, Thin Solid Films **478**, 218 2005.
- [36] W. R. Liu, W. F. Hsieh, C. H. Hsu, Keng S. Liang and F. S. S. Chien, J. Appl. Cryst. **40**, 924, 2007.
- [37] F. A. Ponce, Group III Nitride Semiconductor Compounds: Physics and Applications, edited by B. Gil, 123 Oxford: Clarendon, 1998.

- [38] F. Vigué, P. Vennéguès, S. Vézian, M. Laügt, and J.-P. Faurie, *Appl. Phys. Lett.* **79**, 194, 2001.
- [39] R. Chierchia, T. Böttcher, H. Heinke, S. Einfeldt, S. Figge, and D. Hommel, *J. Appl. Phys.* **93**, 8918, 2003.
- [40] V. Srikant, J. S. Speck, and D. R. Clarke, *J. Appl. Phys.* **82**, 4286, 1997.
- [41] T. Metzger, R. Hopler, E. Born, O. Ambacher, M. Stutzmann, R. Stommer, M. Schuster, H. Gobel, S. Christiansen, M. Albrecht, and H.P. Strunk, *Philos. Mag. A*, **77**, 1013, 1998.
- [42] A. Teke, Ü. Özgür, S. Dogan, X. Gu, H. Morkoç B. Nemeth, J. Nause, and H. O. Everitt, *Phys. Rev. B* **70**, 195207, 2004.
- [43] Y. F. Chen, D. M. Bagnall, H. J. Koh, K. T. Park, K. Hiraga, Z. Zhu, and T. Yao, *J. Appl. Phys.* **84**, 3912, 1998.
- [44] A. Teke, U. Ozgur, S. Dogan, X. Gu, H. Morkoc, B. Nemeth, J. Nause, and H. O. Everitt, *Phys. Rev. B* **70**, 195207, 2004.
- [45] W. J. Shen, J. Wang, Q. Y. Wang, Y. Duan, and Y. P. Zeng, *J. Phys. D: Appl. Phys.* **39**, 269, 2006.
- [46] F. K. Shan, G. X. Liu, W. J. Lee, and B. C. Shin, *Appl. Phys. Lett.* **101**, 053106, 2007.